Atmospheric Research 201 (2018) 17–33

Contents lists available at ScienceDirect

Atmospheric Research

journal homepage: www.elsevier.com/locate/atmosres

Fuzzy-logic detection and probability of hail exploiting short-range X-band weather radar

Vincenzo Capozzi[a,*], Errico Picciotti[b], Vincenzo Mazzarella[a], Frank Silvio Marzano[b,c], Giorgio Budillon[a]

[a] Department of Science and Technology, University of Naples "Parthenope", Centro Direzionale di Napoli, 80143, Italy
[b] Centre of Excellence CETEMPS, University of L'Aquila, 67100, Italy
[c] Dept. of Information Engineering, Sapienza University of Rome, 00184, Italy

ARTICLE INFO

Keywords:
Weather radar
X-band
Hailstorm
Detection methods
Data processing
Urban hydrometeorology

ABSTRACT

This work proposes a new method for hail precipitation detection and probability, based on single-polarization X-band radar measurements. Using a dataset consisting of reflectivity volumes, ground truth observations and atmospheric sounding data, a probability of hail index, which provides a simple estimate of the hail potential, has been trained and adapted within Naples metropolitan environment study area. The probability of hail has been calculated starting by four different hail detection methods. The first two, based on (1) reflectivity data and temperature measurements and (2) on vertically-integrated liquid density product, respectively, have been selected from the available literature. The other two techniques are based on combined criteria of the above mentioned methods: the first one (3) is based on the linear discriminant analysis, whereas the other one (4) relies on the fuzzy-logic approach. The latter is an innovative criterion based on a fuzzyfication step performed through ramp membership functions. The performances of the four methods have been tested using an independent dataset: the results highlight that the fuzzy-oriented combined method performs slightly better in terms of false alarm ratio, critical success index and area under the relative operating characteristic. An example of application of the proposed hail detection and probability products is also presented for a relevant hail event, occurred on 21 July 2014.

1. Introduction

Metropolitan areas are more and more prone to impact of severe convective events, such as hailstorms, convective outbreaks, wind storms and, in some cases, thunderstorms (e.g., Baumgart et al., 2008; Changnon, 2001; Doswell et al., 2006; Dotzek et al., 2009; Farnell et al., 2017; Gatlin and Goodman, 2010; Kunkel et al., 2013; Marzano et al., 2012; Rigo and Pineda, 2016; Roberts et al., 2006; Schultz et al., 2009; Schuster et al., 2006; Tilford et al., 2002; Tuovinen et al., 2009). The increase of urban meteorological risk is due not only to the growth of precipitation intensity in terms of temporal and spatial patterns (very often attributed to the effect of climate change at regional scales), but also to the growing vulnerability of metropolitan infrastructures and settlements (Koussis et al., 2003; Llasat et al., 2009; Llasat et al., 2008). In this respect, civil protection can be more effective if prevention actions and observation systems are planned in advance (Komendantova et al., 2014).

The weather radars have been involved in the development of severe events monitoring and nowcasting techniques: the radar observations, in fact, have been used to implement extrapolation methods, which include cross-correlation tracking (e.g. Lai, 1999; Li et al., 1995) and centroid tracking (e.g. Han et al., 2009; Handwerker, 2002) methods. Moreover, some nowcasting applications rely on the optimal merging between radar data and rain-gauge measurements (e.g. Erdin et al., 2012). However, nowadays, the nowcasting and monitoring system have involved also the use of satellite data (e.g. Mecikalski and Bedka, 2006; Sieglaff et al., 2013), as well as the one of numerical weather prediction models (e.g. Sun et al., 2014; Weisman et al., 2008). The use of weather radar is also of interest for the modelling of urban drainage, since high-resolution rainfall estimates can be used as suitable inputs for forecast systems (Berenguer and Sempere Torres, 2012; Villarini et al., 2010).

The usefulness of weather radar in urban environments can be also exploited for near real-time detection of hail precipitation (e.g. Matrosov et al., 2013), one of the most diffuse and harmful convective hazard. Hail events are typically highly localized, due to their

* Corresponding author.
E-mail address: vincenzo.capozzi@uniparthenope.it (V. Capozzi).

http://dx.doi.org/10.1016/j.atmosres.2017.10.006
Received 16 March 2017; Received in revised form 15 September 2017; Accepted 9 October 2017
Available online 14 October 2017

significant time-space variability (Farnell et al., 2016; Sánchez et al., 1996; Sioutas et al., 2009), and can be monitored, with ground observational networks, only through hailpads and/or electronic hail detection sensors (Löffler-Mang et al., 2010; Morgan and Towery, 1975). However, the widespread diffusion of those networks is limited by management problems (hailpads) and high costs (electronic sensors). As discussed by Kunkel et al. (2013), hail and all severe convective hazards, including tornadoes and thunderstorm winds, are considered in the lowest category of detection knowledge. Most of available information on hailstorms and their occurrence is typically derived from hailstorm reports provided by volunteers (Allen and Tippett, 2015; Schuster et al., 2005; Tuovinen et al., 2009). These reports are inevitably subjected to biases, determined by population density and local circumstances. Weather radars appear to be invaluable instruments for detection and estimation of hail, also because their volumetric scan allows probing the vertical extension of thunderstorm cells. The latter constitutes a key-information for hail detection targets: as highlighted by Delobbe et al. (2003), in fact, there is a relevant connection between the vertical development of a convective cloud and its severity.

Nowadays, the most-innovative approaches developed to distinguish between raindrops and hailstones take advantage of dual-polarization weather radar features (e.g. Aydin et al., 1986; Bechini and Chandrasekar, 2015; Chandrasekar et al., 2013; Marzano et al., 2007, 2010; Picciotti et al., 2013; Straka et al., 2000; Vulpiani et al., 2015), which allow to detect the hail precipitation through the differential reflectivity and the others polarimetric parameters. The only measure provided by single-polarization weather radars, apart from Doppler moments, is the horizontally-polarized reflectivity (Z), which do not allow discriminating among different types of hydrometeors. However, some features in Z measurements, such as the occurrence of high reflectivity cores above the melting layer height (e.g. Burgess and Lemon, 1990; Donavon and Jungbluth, 2007) and the appearance of a particular radar signature, named “flared-echo” or “three-body scatter signature” (e.g. Lemon, 1998; Zrnić, 1987), can be used as proxies of the physical processes related to the hail growth (Kunz and Kugel, 2015; Puskeiler et al., 2016; Skripniková and Řezáčová, 2014).

Several techniques for identifying hailstorms from single-polarization radar measurements have been proposed; an extended overview can be found in Holleman (2001), as well as in Skripniková and Řezáčová (2014). Mason (1971) developed a simple criterion for hail detection, based on the occurrence of reflectivity cores > 55 dBZ; this method has been successfully applied and tested in subsequent studies (e.g. Hohl et al., 2002; Schuster et al., 2006). Some approaches have exploited threshold values for a hail-related quantity, such as reflectivity in low-level constant-altitude plan-position-indicator (CAPPI) data (Geotis, 1963), vertically-integrated liquid density (Amburn and Wolf, 1997) or the difference in altitude between the height attained by 45-dBZ reflectivity core and the freezing level (Waldvogel et al., 1979). Witt et al. (1998) determined a probability function for severe hail, evaluating the performance of a hail detection algorithm based on Waldovogel's method. Holleman (2001), using different source of on-ground observations, such as synoptic stations, agricultural insurance companies, reports from weather amateurs and newspapers, verified the performance of eight different hail detection products. Several studies have proposed a merge between radar data and other meteorological measurements, such as aerological data and infrared cloud-top temperatures from satellite imagery (Auer, 1994; Hohl et al., 2002; Kunz and Kugel, 2015; Waldvogel et al., 1979; Witt et al., 1998). An interesting hail identification technique has been considered by Ceperuelo et al. (2009), based on kinetic energy flux as a discrimination between hail and no-hail precipitation in the studied area. Recently, Skripniková and Řezáčová (2014) have tested some of the hail detection criteria just mentioned for both Czech Republic and Germany. Kunz and Kugel (2015) have evaluated hail signals from C-band single-polarization radar features both for single cases and over a 15-years period in the southwestern Germany. An estimation of the hail signals in the whole Germany has been also provided by Puskeiler et al. (2016), which have applied the algorithms developed by Mason (1971) and Waldvogel et al. (1979). Nisi et al. (2016) present a 13-years hail climatology for Switzerland and adjacent countries, using two radar-based hail detection products, the probability of hail and the Maximum Expected Severe Hail Size. The latter have been computed using the highest altitude at which a radar reflectivity of at least 45 and 50 dBZ can be detected.

Most of single and dual-polarization fixed weather radars operate at S-band (3-cm wavelength) and at C-band (5-cm wavelength); however, such systems require a high cost for purchasing, as well as for infrastructure and maintenance. An appealing alternative to S-band and C-band fixed systems is represented by X-band radar systems. Although the latter are limited in their capabilities by beam attenuation along the path, at short-range they may exhibit performance comparable with conventional systems, but typically with lower purchasing, installation and maintenance costs (Montopoli et al., 2010; Van de Beek et al., 2010). The latter characteristics render X-band systems very appealing for the development of products and applications useful for severe weather surveillance in urban areas and small-scale basins (e.g., Anagnostou et al., 2004; Bechini et al., 2013; Figueras i Ventura et al., 2013; Marzano et al., 2010, 2012; Matrosov et al., 2005; Montopoli et al., 2010; Van de Beek et al., 2010).

This work, using single-polarization X-band reflectivity data, aims to develop an innovative hail detection and probability algorithm, named hailstorm fuzzy-oriented and detection (HFOD). The latter is based on a merging, performed means of fuzzy logic, of the outcomes of two well-known techniques: the first one exploits the difference of height (DOH) between the altitude attained by a determined reflectivity core and the zero-degree isotherm, as proposed by Waldvogel et al. (1979), whereas the second one is based on the vertically-integrated liquid density (VLD) product, proposed by Amburn and Wolf (1997). The information, provided by these two different hail detection techniques, have been also merged using the Linear Discriminant Analysis, which allows determining a combined criterion (CMB) through a simple linear approach. The four different algorithms (DOH, VLD, CMB and HFOD) have been trained and tested in a pilot study area: the Naples metropolitan environment. The statistical evaluation of the hail detection algorithms has been quantified by using standard verification scores (i.e., probability of detection, false alarm ratio, probability of false detection, critical success index, relative operating characteristic), derived from 2-by-2 contingency table.

This paper has the following structure. Section 2 provides a description of the study area, as well as information about the meteorological scenarios that commonly affected it. Moreover, this section describes the radar data processing and the thunderstorm events examined. The selected algorithms for hail detection are illustrated and discussed in Section 3. The verification scores used in statistical analysis and the results of the study are presented in the fourth section. The latter is devoted also to an application of the hail detection and probability products at a strong hail event occurred in July 2014. Conclusions are finally drawn together with prospects for future research.

2. Area of study, radar data and description of thunderstorm events

This section describes the features of the geographical area of interest and the variability of the considered meteorological scenarios. Moreover, it provides information about weather radar characteristics and the selected database of thunderstorm events.

2.1. Study area and meteorological scenarios

The region of study, located in Southern Italy, includes the Naples metropolitan area (which has a population of about 3 millions of

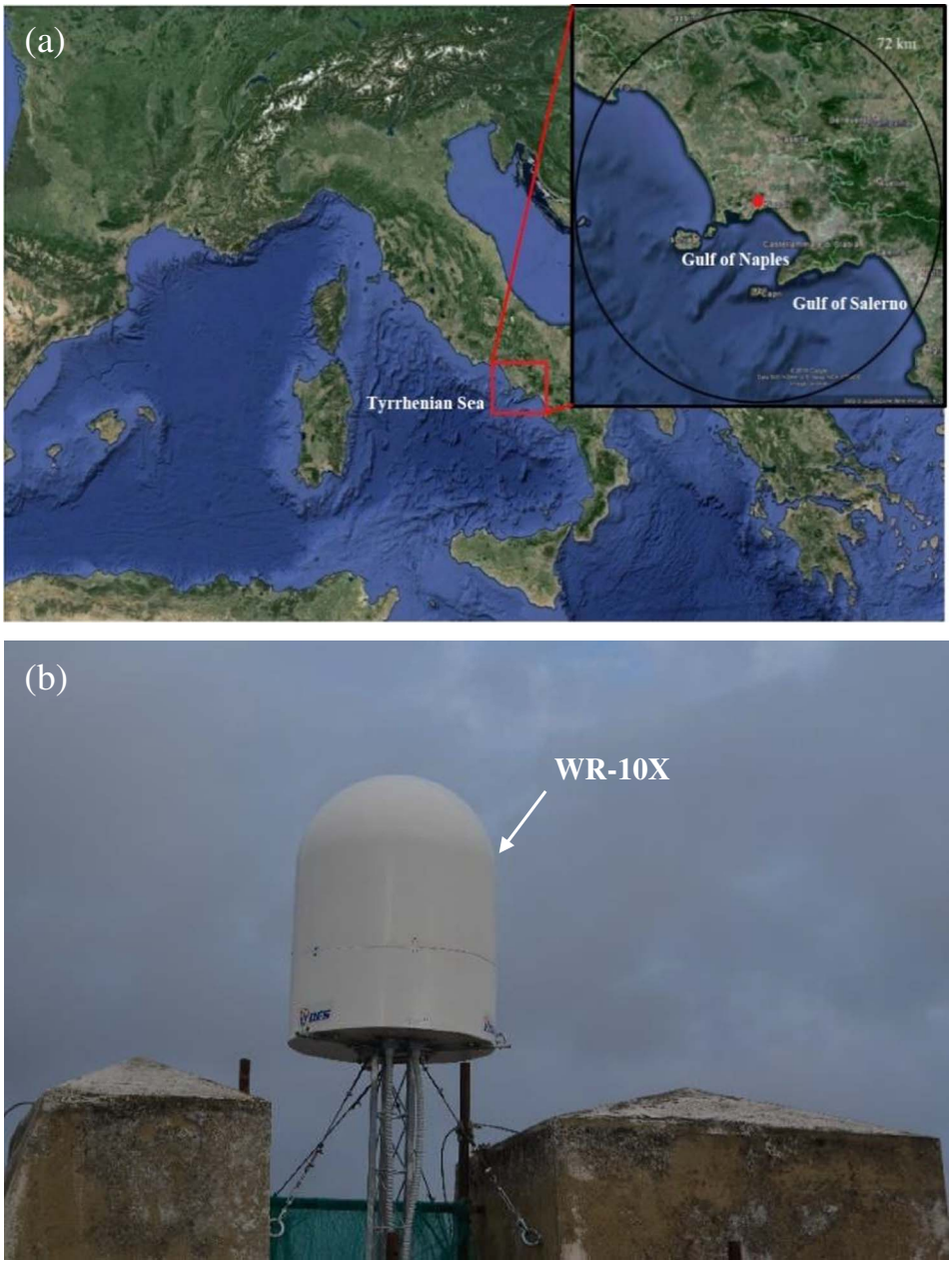

Fig. 1. In (a), a map of study region including radar location (filled-in red circle) is presented. Circular line at 72 km from Naples Castel Sant'Elmo indicates the limit of the area covered by radar. In (b), WR-10X installation at Naples Castel Sant'Elmo Site is shown. (For interpretation of the references to color in this figure legend, the reader is referred to the web version of this article.)

inhabitants), the central and northern coastal sectors of Campania Region, the plain of Caserta and the western side of Campania Apennine reliefs (Fig. 1a).

In cold season (November to April), the convection is usually triggered by cold fronts or cold occlusions, which are associated to the passage of atmospheric transients developed from the polar front. Moreover, in wintertime, the region of interest is sometimes affected by polar maritime air masses, coming from the North-Atlantic. The latter, crossing the relatively warm surface of Tyrrhenian Sea, may experience a heating in their bottom layers. This mechanism can lead to the development of thunderstorm cells over the sea surface, that may affect also the coastal sectors, causing hail (or seldom graupel) precipitation.

The thunderstorm events that affect this area in the warm season (May to October) are mainly triggered by the interaction between small-scale mechanism and synoptic-scale flow. The analysed region is bounded on the north by Matese mountains and on the east by Campania Apennine, which have height values of > 2000 and 1500 m, respectively. These two orographic features constitute an important factor in the mesoscale meteorology of the region, enhancing convection systems development, especially in summer season. During warm season, convection can be even triggered by the low-level convergence between diurnal sea-breeze and synoptic-scale flow, when an unstable environment is present. This mechanism usually occurs in the inland sectors (at a distance of about 20–30 km from the coast) and, in combination with orographic forcing, can cause the development of hail producing thunderstorms.

Sea-air interactions also play a crucial role in storm activity: in the early part of fall season, when sea surface temperatures reach the maximum value ($\cong 26\ ^{\circ}C$), coastal areas are sometimes affected by heavy thunderstorms, that are able to produce considerable rainfall accumulation (> 100 mm) in a relatively short time.

The mechanisms that force convection in our study area are similar to the ones typical of Mediterranean region. As an example, Price and Federmesser (2006) highlight that the Mediterranean winter thunderstorms are associated with synoptic weather systems and that they are in direct link with the location and the intensity of the mid-latitude jet

stream. Lebeaupin et al. (2006) highlight that the Mediterranean sea, still warm in the first part of fall season, can supply moisture and heat to the low-level of troposphere, enhancing the development of convective instability. Moreover, the convergence between sea breeze and large-scale flow has been recognized as an important mechanism for thunderstorm development also in the Iberian Peninsula (Azorin-Molina et al., 2009).

2.2. Radar characteristics and data quality control

An X-band single-polarization weather radar, named WR-10X (Fig. 1b), has been installed in Naples' urban area, on November 2011, at the top of Castel Sant'Elmo (40.8438°N, 14.2385°E, 280 m above sea level). The radar belongs to the meteorological monitoring network of the Campania Center for Marine and Atmospheric Monitoring and Modelling (CCMMMA), which is financed by the University of Naples "Parthenope". The first research activities that have involved WR-10X measurements have addressed topics related to the quality control of radar data and to the improvement of WR-10X quantitative precipitation estimates (Capozzi et al., 2014). Moreover, some preliminary studies have been devoted to generate radar-based hail detection products (Capozzi et al., 2015, 2016; Marzano et al., 2012).

The WR-10X collects reflectivity measurements using a scan strategy that involves six antenna elevation angles, ranging from 1.0 to 10.0°. The volume scan is performed every 10 min, with a pulse repetition frequency of 800 Hz, a resolution in range of 0.3 km and a resolution in azimuth of 3.0°. A complete volume scan is carried out in a time of 3 min for a maximum range of 72 km. The raw Z measurements collected by WR-10X are affected by some common range-dependent and systematic errors, which include the ground and sea clutter, the beam obstruction by mountain reliefs and the beam attenuation along the path. These effects and their correction and/or mitigation are briefly discussed in the following items (a more detailed description can be found in Capozzi et al., 2014):

1. In order to remove the noise caused by ground clutter, a statistical filter has been developed. The latter is based on three main components: entropy, texture and median filtering (Montopoli et al., 2010).
2. The approach used to eliminate sea clutter noise is based on the analysis of vertical reflectivity profiles (Alberoni et al., 2001). Generally, in fact, vertical reflectivity profiles are smooth and regular in rainy conditions, whereas in sea clutter circumstance a broken profile is often detected.
3. In order to minimize the effects of partial beam blockage caused by surrounding topography, we have applied the correction scheme proposed by Fulton et al. (1998). This scheme is applied to beams partially obstructed, i.e. only when the level of beam occultation lies between 10% and 60%, and consists of modifying the reflectivity factor measurements by adding 1 to 4 dBZ depending on the degree of occultation.
4. The two-way attenuation along the path, together with other sources of error, such as calibration errors, side lobe effects, shielding and range-dependent errors, can adversely affect the ability of weather radar to provide accurate measurements of vertical profile of reflectivity (Delobbe and Holleman, 2006). This problem has a significant importance at X-band (e.g. Delrieu et al., 1999a, 1999b) and it is highly dependent on rainfall intensity (Marzano et al., 2003). The WR-10X weather radar, being a single-polarization system, cannot exploit polarimetric capabilities, which allow, nowadays, developing the most efficient approach to estimate the attenuation. Therefore, the beam attenuation along the path has been mitigated through a classical iterative procedure that implicates the assessment of two-way path integrated attenuation (PIA) along the entire beam path. The PIA iterative method has proved to be reliable in attenuation correction within a range (i.e. distance from the radar site) < 50 km; occasional failures of this methodology have been observed in the case of particular meteorological scenarios, characterized by strong rainfall in the range closest to the radar site. The influence of path attenuation on radar-based hail detection techniques performance may be considered relatively low because the radar-based hail detection products, developed in this work, have been tested at urban scales of the order of few tens of kilometres. The incidence of path attenuation along determined radial directions may be regarded as unusual at short distances (Marzano et al., 2012) and, therefore, not influencing the performance of X-band radars, at least from a statistical point of view. In addition, in order to minimize the effects of attenuation, we have focused the selection of thunderstorm events on situations where no other convective cells are present along the radial directions between the radar site and the convective cell of interest.

2.3. Dataset description

The collected database includes 53 thunderstorms that occurred in the study area from April 2012 through June 2015. The 43% of this dataset consists of isolated thunderstorms (single convective cells), whereas the remaining 57% comprises 13 thunderstorm days in which more than one convective cell have been observed and analysed. Unfortunately, the thunderstorm events occurred between March 2013 and June 2014 have not been taken into account, because no radar observations were available in this period due to some technical issues suffered by WR-10X.

Some thunderstorms events that took place within the cone of silence (that is, near to the radar site) have been discarded, since WR-10X is not able to scan the upper part of the thunderstorm. This problem assumes a special significance when the convective cells have a great vertical extension, as often happens in warm season. Therefore, the events close to the radar site (at a distance < 15 km) have been taken into account only if they occurred in the cold season, when, on average, the convective cells have a limited vertical extension. Several thunderstorm events occurred in the south-eastern azimuth of the study area have been discarded, since WR-10X beam is obstructed at lower elevation by the volcano Vesuvio. Moreover, the relatively broad beamwidth of WR-10X suggests to reject most of the thunderstorm events occurred at great distance (> 50 km) from the radar site. The lobe width, in fact, may determine an oversampling of the cloud structure (i.e. a certain reflectivity value could be sampled by more than one radar beam) and, consequently, may adversely affect the successful implementation of the hail detection techniques involved in this study.

The location of the on-ground observations and reports of thunderstorm events is presented in Fig. 2. To better emphasize the seasonal difference in spatial distribution of thunderstorm events location, a map for cold season (Fig. 2a) and a map for warm season (Fig. 2b) have been drawn up. Different markers have been used in Fig. 2 to highlight the different verification data types used. The Synop data have been all provided by Napoli/Capodichino manned station (40.8848°N, 14.2917°E, 72 m a.s.l.), located at a distance of about 6 km from radar site and belonging to the "Meteorological Service of Military Italian Aeronautics". In order to identify the occurrence of thunderstorms through the Synop observations, we have considered the field of Synop message named "Present and Past Weather Group reported from a manned weather station". The latter includes both information about the weather phenomena observed at the time of the observation (the "Present weather") and about the weather phenomena occurred in the previous three or 6 h (the "Past weather"). For the purposes of this study, we have taken into account only the observation related to the present weather, which is associated to a precise temporal information. The past weather observations, in fact, although may be useful to identify the occurrence of thunderstorms in the study area, do not contain specific information about the time in which the weather phenomenon is occurred. Therefore, the eleven Synop reports included

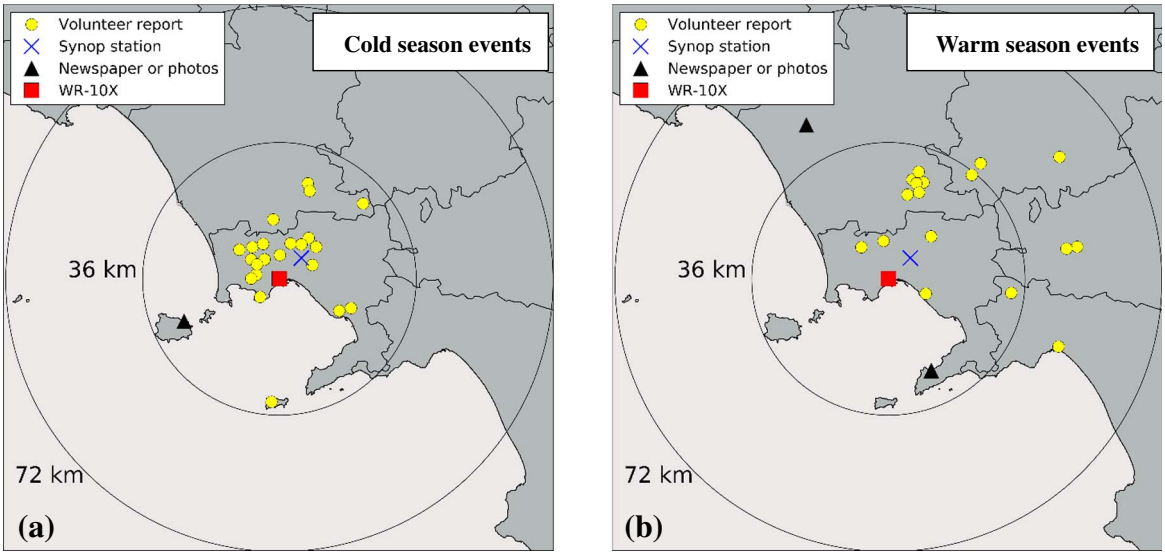

Fig. 2. Location of on-ground observations and reports of thunderstorm events occurred in the study area in the cold season (a), i.e. from November to April, and in the warm season (b), i.e. from May to October. The hail reports provided by volunteers are marked as filled-in yellow circle, those provided by Synop observations as blue cross and the reports from local newspaper as filled-in black triangle. The Synop observations (eleven in all) have been all provided by Napoli/Capodichino station (40.8848°N, 14.2917°E). WR-10X location is highlighted as filled-in red square. (For interpretation of the references to color in this figure legend, the reader is referred to the web version of this article.)

in the dataset are referred to the Present Weather observations: all of these have reported the occurrence of thunderstorms without hail.

Due to the limited spatial and temporal extension of hailfall phenomena, the conventional Synop observations reported only a minor fraction (the 21%) of the overall number of events. For this reason, the ground truth data include also the spotter's observations and the reports provided by local daily newspapers. The spotters' data constitute a high valuable information both for studies devoted to the hail climatology reconstruction (e.g. Kahraman et al., 2016; Tuovinen et al., 2009) and for the development of radar-based hail detection products (e.g. Lahiff, 2005; Wyatt and Witt, 1997). The spotters' data, used in this study, have been retrieved by a web community of weather amateurs (http://www.campanialive.it). The observations about the occurrence of meteorological phenomena are reported by the spotters in the form of message boards and include both temporal and spatial information. Sometimes, video or photographic evidences of the weather phenomena that are taking place accompany the textual message. It should be noted that the spatial and temporal information are not always indicated accurately. Therefore, the criterion used to accept or reject the spotters' data is mainly based on the availability, for a determined observation, of precise information about the place (geographical coordinates) and time (year, month, day, hour and minute).

It should be also highlighted that the spatial distribution of the spotters in region covered by WR-10X is not homogeneous, due to the strong difference in population density between the Naples metropolitan area and the inland sectors. According to the mesoscale meteorology of the study area, this inhomogeneity in spotters' spatial distribution might have determined the non-inclusion, in the considered database, of some thunderstorm events occurred in the warm season (which typically affect the inland sectors). Moreover, it is important to point out that the criterion used to select the thunderstorm events, based on precise time and spatial information, may have determined the non-inclusion, in our database, of some no-hail bearing storms. The latter, in fact, lasting much more than hailstorms, may be difficult to identify with a precise time information. Due to this potential bias, our database may not reflect the natural climatology of thunderstorm events in the study area.

The available thunderstorms database has been divided into a 60% training dataset and 40% test dataset. The training set has been used to optimize each of the four proposed algorithms, whereas the test dataset has been considered for verifying the proposed algorithms. Even though this choice reduces the number of test samples, at the same time it allows the parameter tuning and the preliminary evaluation of the robustness of the optimized hail detection techniques. The training dataset includes 20 thunderstorm events that produce hail precipitation and 11 convective events in which only heavy rain has been observed. The test dataset consists of 22 events, with the same proportion of hail-producing and no hail-producing thunderstorms.

3. Radar techniques for hail detection and retrieval methodologies

Four hail detection algorithms are here illustrated from a methodological point of view. Moreover, this section provides some information about the statistical scores used to evaluate the performance of the four developed techniques.

3.1. Difference of height (DOH) method

The DOH technique, introduced by Waldvogel et al. (1979), evaluates the difference ΔH, expressed in km, between the maximum altitude (H_{ZT}) attained by a determined horizontally-polarized reflectivity core T (in dBZ) and the zero-degree isotherm height (H_{T0}):

$$\Delta H = H_{ZT} - H_{T0} \quad (1)$$

This method takes into account two elements of major relevance in the framework of hail formation process. The first one is the occurrence of a relevant updraft, whose proxy is the altitude of a strong reflectivity core. The second one is the presence of a considerable amount of supercooled liquid water and/or ice, whose proxy is the height of the sharp reflectivity core above the zero-degree level.

The criterion developed by Waldvogel et al. (1979) has been tested in Kessinger et al. (1995) and has been included in the hail detection algorithm developed by Witt et al. (1998). Moreover, the performance of DOH method has been evaluated by Holleman (2001) on a large verification dataset, which includes the hail events occurred in Netherlands from 1999 to 2000. Using the results of this verification analysis, Holleman (2001) has developed a relationship between ΔH and the probability of hail precipitation; this relationship, based on a linear equation (Delobbe et al., 2003; Holleman, 2001), is currently used operationally at KNMI (Royal Netherland Meteorological Institute) and

in other meteorological services. The results achieved by this study have also highlighted that the DOH method is more suitable for the identification of summer hail events than the winter ones, due to the seasonal variability of ΔH. More recently, the Waldvogel criterion has been optimized by Skripniková and Řezáčová (2014) for the Czech territory.

The DOH method, although implies a merging between radar reflectivity measurements and other types of meteorological data, has the advantage of a very simple implementation. However, the performance of this methodology can be adversely affected by some limitations, caused by radar beam size and the finite number of elevation scans, which may determine errors in the height assigned to the measured reflectivity values (Delobbe and Holleman, 2006; Lakshmanan et al., 2013).

In this work, the freezing level has been assessed through a linear interpolation of the radiosonde data acquired at Pratica di Mare (41.67°N, 12.45°E), which is the sounding station nearest to the study region. Pratica di Mare is located outside the area covered by WR-10X measurements, at a distance of 150 km from Naples. In order to prove the reliability of this station for the purposes of our work, we have compared the H_{T0} data provided by Pratica di Mare soundings with the ones predicted by the Limited Area Model implemented by the Centre of Excellence "CETEMPS" of the University of L'Aquila. The considered numerical prediction model is based on the Weather Research and Forecast (WRF) system and has a spatial resolution of 6 km. The WRF domain used for the comparison includes the entire area covered by WR-10X and contains a total of 572 grid points. The comparison has been performed with respect to a sample of 25 thunderstorm events, belonging to the dataset used in our analysis.

For the considered events, we have taken into account the vertical temperature profiles predicted by WRF model at the integration time closest to the one in which the thunderstorm has been observed or reported. For each event, the H_{T0} estimates provided by WRF model have been spatially averaged, over the considered domain, and compared with those provided by Pratica di Mare soundings. The results (Fig. 3) show a good fit between the two datasets, as pointed out by Pearson correlation coefficient (= 0.95), by Root Mean Square Error (= 0.25 km) and by the slope of the linear regression model (= 0.9132) values; the difference between the two estimates of H_{T0} is generally negligible, except for few events occurred in the cold season. Moreover, for the selected 25 events, we have compared the vertical temperature profiles measured at Pratica di Mare at 00:00 and 12:00 UTC and the ones predicted by the WRF model, at same times, in the grid point nearest to the radar site. The evaluation of simple statistical indicators, such as the Pearson correlation coefficient (= 0.99), the BIAS

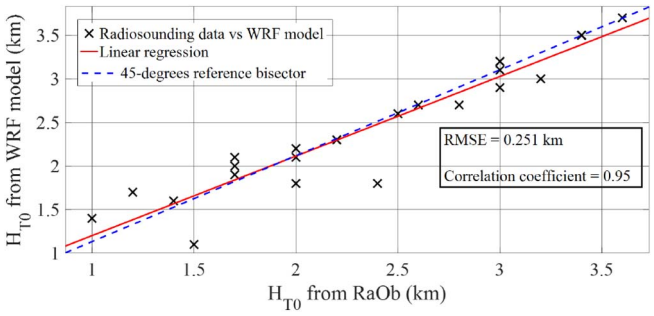

Fig. 3. A comparison between the freezing level (H_{T0}) predicted by CETEMPS WRF model, averaged over all grid points of the considered domain, and the freezing level estimated by Pratica di Mare sounding data is presented. The superimposed text box contains the values of Pearson correlation coefficient and Root Mean Square Error (RMSE). The red solid line represents the linear regression, whereas the blue dashed line indicates the 45° reference bisector. The scatter plot shows the results obtained for 25 thunderstorm events, belonging to the dataset used in this study. (For interpretation of the references to color in this figure legend, the reader is referred to the web version of this article.)

(= 0.45 K) and the standard deviation (= 1.91 K), clearly demonstrates the very good agreement between Pratica di Mare sounding measurements and WRF data.

Note that, not only the best threshold value for ΔH (i.e. a threshold that properly distinguishes between hail and severe rain) is important for the aims of this study, but also the reflectivity core where the DOH method exhibits the finest performance for our study area and our radar features. In this respect, the Eq. (1) has been computed not only considering the original criterion proposed by Waldvogel et al. (1979), which implies the use of H_{Z45}, but also as a difference between the maximum height attained by 35 and 40-dBZ reflectivity cores (named H_{Z35} and H_{Z40}) and H_{T0}.

3.2. Vertically-integrated liquid density (VLD) method

The vertically integrated liquid (VIL) product provides an instantaneous estimate of the water content accumulated in an atmospheric layer. VIL has been proposed as an index of storm cell severity by Greene and Clark (1972) and converts horizontally-polarized reflectivity measurements Z into equivalent liquid water mass content (M_e) via a semi-empirical power-law relation between M_e, in kg m^{-3}, and Z, in mm^6 m^{-3}, that is $M_e = aZ^b$.

The VIL product, expressed in kg m^{-2}, is obtained by integrating M_e along the vertical coordinate h (expressed in m) of each column within the observed radar volume. The main issues that have to be taken into account when deriving the VIL are described in detail by Brimelow et al. (2004) and by Delobbe and Holleman (2006).

The VIL Density (VLD) tool as hail indicator has been proposed by Amburn and Wolf (1997), in order to mitigate the weaknesses of VIL product. VLD can be obtained dividing VIL by H_{TOP}, as defined in Eq. (2):

$$VLD = 1000(VIL/H_{TOP}) = 1000(a/H_{TOP}) \int_0^{H_{TOP}} [Z(h)]^b dh \quad (2)$$

where the factor 1000 is used in order to express VLD in g m^{-3} and the H_{TOP} (expressed in m) is the altitude of the highest echo detected by radar, also called *EchoTOP* product. VLD correlates well with storm cell containing hail cores, since those thunderstorms are usually characterized by high reflectivities at relatively high altitudes. This is, indeed, also a limitation of VLD algorithm since weather radars are not able to observe hail close to the ground. This problem may occur in circumstances of quite high freezing levels or if the hailstones fall through significant liquid water particles. It should be noted that the VLD product, normalizing the reflectivity with respect to the EchoTOP, is less sensitive than DOH method to the thunderstorm vertical extension.

In order to optimize the performance of VLD tool for the purposes of this work, a sensitivity analysis has been performed, computing the Eq. (2) through three different pairs of coefficients (a, b): $a = 3.44 \cdot 10^{-6}$ and $b = 4/7$ (Greene and Clark, 1972), $a = 6.56 \cdot 10^{-6}$ and $b = 0.54$ (Maki et al., 2005), $a = 9.64 \cdot 10^{-7}$ and $b = 0.693$ (Maki et al., 2005). The VLD products obtained means of these three set of coefficients are named VLDa, VLDb and VLDc respectively.

3.3. Combined (CMB) criterion

The DOH and VLD algorithms, once optimized through a statistical analysis that will be described in Section 4, have been combined into two different criteria: the first one, named CMB method and briefly discussed in this paragraph, has been introduced to evaluate what is the best result that can be achieved combining the two canonical techniques with a simple linear approach. The second one, named HFOD, is illustrated in the next subsection.

The set-up of CMB criterion is based on the Linear Discriminant Analysis (LDA) technique. The latter is a robust classification method, originally developed by Fisher (1936). The aim of LDA analysis is to

search for a linear combination of variables (predictors) that best discriminate among different types of objects or classes.

From a mathematical perspective, given two different classes, the hail (*HE*) and the no-hail (*NHE*) events in our case, and two different predictors, e.g. ΔH and VLD, the problem consists in estimating the linear coefficients β_1 and β_2 that maximize the following score function, defined by Fisher (1936):

$$S(\beta) = \frac{\beta^T \mu_{HE} - \beta^T \mu_{NHE}}{\beta^T C \beta} \tag{3}$$

where μ_{HE} and μ_{NHE} are the mean vectors, computed with respect to *HE* and *NHE* classes, β is the coefficients vector and C is the pooled covariance matrix. The score function can be maximized through the following equations:

$$C = \frac{1}{n_1 + n_2}(n_1 C_{HE} + n_2 C_{NHE}) \tag{4}$$

$$\beta = C^{-1}(\mu_{HE} - \mu_{NHE}), \tag{5}$$

where C_{HE} and C_{NHE} are the covariance matrices, determined with respect to *HE* and *NHE* classes. n_1 and n_2 are the number of ΔH and VLD observations belonging to the classes *HE* and *NHE*, respectively.

Once determined the coefficients β_1 and β_2, the LDA estimator, named Φ, can be easily applied as follows:

$$\Phi = \beta_1 \Delta H + \beta_2 VLD \tag{6}$$

The LDA analysis has been performed using the optimized outcomes of DOH and VLD criteria as predictive variables.

3.4. Hail fuzzy-logic oriented detection (HFOD) method

The HFOD criterion combines the optimized DOH and VLD methods through the fuzzy logic approach. The latter is a powerful problem solving technique with large applicability, belonging to the family of cognitive computing algorithms.

The available literature offers various examples of fuzzy logic schemes developed for hydrometeors identification purposes, mostly based on dual polarization weather radars (e.g., Heinselman and Ryzhkov, 2006; Liu and Chandrasekar, 2000; Mahele et al., 2014; Marzano et al., 2007; Park et al., 2009; Zrnić et al., 2001).

In the current application of fuzzy logic method, the systems input (i.e. the physical variables that are supposed to determine the solution of the problem) are Δ*H* and VLD, which are the outcomes of the optimized DOH and VLD techniques, respectively, whereas the system output is the POH. The fuzzyfication step has been performed through ramp membership functions. The analytic expression of the two ramp functions introduced in this work, named $M_{\Delta H}$ and M_{VLD}, is:

$$M_{\Delta H}(\Delta H, \Delta H_1, \Delta H_2) = \begin{cases} 0, & \Delta H \le \Delta H_1 \\ \frac{\Delta H - \Delta H_1}{\Delta H_2 - \Delta H_1}, & \Delta H_1 < \Delta H \le \Delta H_2 \\ 1, & \Delta H > \Delta H_2 \end{cases} \tag{7}$$

$$M_{VLD}(VLD, VLD_1, VLD_2) = \begin{cases} 0, & VLD \le VLD_1 \\ \frac{VLD - VLD_1}{VLD_2 - VLD_1}, & VLD_1 < VLD \le VLD_2 \\ 1, & VLD > VLD_2 \end{cases} \tag{8}$$

where ΔH and VLD are the input values, ΔH_1 and VLD_1 the starting points of the ramp functions and, finally, ΔH_2 and VLD_2 the end points of the same.

The inference rule, which constitutes the core of the fuzzy logic system, is based on a weighted linear combination of the two ramp membership functions:

$$M(\Delta H, VLD) = w_1 M_{\Delta H}(\Delta H, \Delta H_1, \Delta H_2) + w_2 M_{VLD}(VLD, VLD_1, VLD_2) \tag{9}$$

where w_1 and w_2 are the weight factors of $M_{\Delta H}$ and M_{VLD}, respectively. The variability range of M(ΔH, VLD) is between 0 (no probability of hail) and 1 (certainty of hail); therefore, the sum of the weight factors must be equal to 1.

In order to determine the optimal inference function (hereafter, M_{OPT}), the inference function M(ΔH, VLD) has been tested in the framework of the verification analysis for several combinations of the following parameters: w_1, w_2, ΔH_1, ΔH_2, VLD_1 and VLD_2. The HFOD optimization will be described in the following Section 4, based on the selected training dataset.

3.5. Statistical score indexes

The four hail detection methodologies above described have been applied using the WR-10X corrected reflectivity measurements. To implement DOH method, the maximum altitude attained by each of the three reflectivity cores tested in this study (35, 40 and 45-dBZ) has been searched for every radar bin of each volume scan. Once determined this quantity, i.e. the term H_{ZT} in Eq. (1), the product ΔH has been computed using the H_{T0} information provided by Pratica di Mare sounding data. However, for some radar bins, the computation of ΔH may be not possible, due to the unavailability of the reflectivity cores at 35, 40 and 45-dBZ.

The first step of VLD algorithm computation involves the conversion of corrected *Z* measurements into M_e; the latter has been retrieved using three different pairs of (a, b) coefficients. The subsequent step implies the integration of M_e over the vertical column, in order to determine the VIL. Finally, VLD product has been computed dividing the VIL values by *EchoTOP* altitudes, according to Eq. (2). The WR-10X polar volumes have been resampled into a uniform Cartesian grid with 0.3-km horizontal resolution before the calculation of DOH and VLD outcomes.

The implementation of CMB technique has been performed applying the Eqs. (4), (5) and (6), in order to determine the best coefficients of the linear model that combines the optimized DOH and VLD criteria. The set-up of HFOD method follows the computation of DOH and VLD, by selecting the optimal weights parameters of the fuzzy-logic algorithm in Eqs. (7), (8) and (9). Note that all radar products described in this manuscript have been performed by means authors' developed algorithms.

The comparison between radar products (computed in each pixel of WR-10X coverage's domain) and ground-truth observations, that primarily pursues the aim to determine a warning threshold which is able to discriminate between hail and rainfall, has been performed applying both a temporal and spatial tolerance. The temporal mismatching issues have been mitigated considering not only the WR-10X volume scan collected at the time (t_n) closest to that of the on-ground observation, but also the previous and the next WR-10X volume scans, i.e. the reflectivity data acquired 10 min before and after the time t_n, respectively. Among these three WR-10X volume scans, the one with the highest ΔH and VLD values within a tolerance distance of 15 km from on-ground observation location has been taken into account.

According to Holleman (2001), the thunderstorms events have been classified using a 2-by-2 contingency table (Table 1). The meaning of symbolisms adopted in Table 1 is explained below:

- *H* (hit) is an integer that represents the number of times that a hail event is identified by a radar-based methodology and is observed by ground truth reports;
- *F* (false alarm) is an integer that represents the number of times that a hail event is identified by a radar-based technique and is not observed by ground truth reports;
- *M* (miss) is an integer that represents the number of times that a hail event is not identified by a radar-based methodology and is observed by ground truth reports;
- *N* (corrected negative) is an integer that represents the number of times that a hail event is not identified by a radar-based technique

Table 1
Contingency table used in the comparison between the outcomes of the radar-based hail detection methods and the ground truth verification data.

		Has the hail event been detected by radar?		
		Yes	No	
Has the hail event been observed on the ground?	Yes	H (hits)	M (misses)	Total number of events observed on ground H + M
	No	F (false alarms)	N (corrected negatives)	Total number of events not observed on ground F + N
		Total number of hail events detected by radar H + F	Total number of hail events not detected by radar M + N	Total number of events H + F + M + N

and is not observed by ground truth reports.

In this work, it is assumed that a hail event is detected by a radar-based method, e.g. the DOH technique, when ΔH is above a certain threshold. In order to find the optimal warning thresholds for hail warning in Naples urban area, the contingency table has been computed for several values of ΔH, ranging from 0.2 and 3.0 km, and for several VLD values, ranging from 1.4 to 5.6 g m^{-3}. By adopting the outcomes of the 2-by-2 contingency table, the following statistical scores have been computed:

$$\begin{cases} \text{Probability of detection (POD)} = H/(H+M) \\ \text{False alarm ratio (FAR)} = F/(H+F) \\ \text{Probability of false detection (POFD)} = F/(F+N) \\ \text{Critical success index (CSI)} = H/(H+M+F) \\ \text{Probability of hail (POH)} = H/(H+F) = 1 - \text{FAR} \end{cases} \quad (10)$$

The CSI well summarizes the verification result and has been mainly used to establish a good warning threshold. Moreover, the performance of the four different trained algorithms has been assessed also in terms of the area under the relative operating characteristic (ROC) graph. The latter is a simple and very useful tool used to visualize and evaluate different classifiers based on their performance (Fawcett, 2006). The ROC graph is a two-dimensional plot, in which the POD score is plotted on y-axis and the POFD score on x-axis: therefore, according to Fawcett (2006), the ROC graph depicts the relative trade-off between costs (i.e. the false positives) and the benefits (i.e. the true positives). In order to compare the performance of different classifiers, the information provided by the ROC graph can be synthetized into a single scalar value, the area under the ROC curve (e.g. Bradley, 1997). The ROC curve area values range from 0 to 1: a perfect classifier has an area of 1, whereas no reliable classifiers have an area < 0.5.

4. Results and applications to a case study

This section introduces the set-up of the proposed single-polarization X-band techniques for estimating the probability of hail (POH) and, as an example, its application at the hail event occurred on July 21, 2014. This event belongs to the dataset used to test the POH products developed in this study.

4.1. Sensitivity analysis and algorithm training

The complete list of the thunderstorm events belonging to the training dataset is presented in Table 2. The latter contains the following information: distance from the radar site (R) of the on-ground observation of the thunderstorm, H_{TOP}, H_{T0}, H_{Z35}, H_{Z40}, H_{Z45} and VLD values determined from the three VLD products tested in this study (VLDa, VLDb and VLDc). It is important to point out that the H_{TOP}, H_{Z35}, H_{Z40}, H_{Z45} and VLD values reported in Table 2 have been computed within 15-km distance from the location where the on-ground observation of the thunderstorm event has been reported.

According to Table 3, which is also referred to the training dataset, the convective events occurred in warm season have greater ΔH and VLD median values than those found for cold season. Consequently, the warm season thunderstorm events, developing in a hot and moist environment and having a deeper vertical extension, are more prone to produce dangerous hailstones. The convective events occurred between November and April, although sustained by weaker updrafts, develop into a colder environment (i.e. a great portion of the cumulonimbus cloud have sub-freezing temperature). Therefore, the winter thunderstorm can still enhance the formation of hailstones, albeit generally of lower size and less harmful than those typical of warm season. Moreover, as expected, the number of thunderstorm events without hail reduces with increasing of ΔH and VLD values. For ΔH values greater of 1.0 km and for VLD values greater of 3.5 g m^{-3}, almost all thunderstorm events produced hail precipitation, whereas for ΔH < 1.0 km and VLD < 2.5 g m^{-3}, most of the observed thunderstorms did not cause hail.

The peculiarities of hail events involved in this study are consistent with those emerged from works carried out in other regions of Europe. Holleman (2001), analyzing a dataset of thunderstorm events collected in Netherlands, highlights the difference between the summer hail, which is usually characterized by relatively high size, and the winter hail, which is typically of small size and less dangerous. Tuovinen et al. (2009), in a study devoted to the analysis of the climatology of severe hail in Finland, concluded that large hail occurs mainly between May and mid-September. Moreover, according to Kahraman et al. (2016), severe hail events occur in Turkey mainly between mid-April and mid-June.

The results, achieved from the training of the DOH and VLD algorithms, are summarized in Figs. 4 and 5. The latter show the behaviour of the score indexes values (POD, FAR, CSI and POH) as a function of ΔH and VLD thresholds. As a general result, a gradual lowering of FAR and POD scores with increasing of thresholds has been observed. Moreover, the CSI score index maximizes at a certain value, that has been considered the discriminatory threshold for distinguish between hail occurrence and rainfall.

Among the three variants of DOH method tested in study, hereafter named DOH 35-dBZ, DOH 40-dBZ and DOH 45-dBZ, the one using the 40-dBZ reflectivity core has exhibited the best performance in terms of CSI index (Fig. 4). For DOH 40-dBZ criterion, the CSI reaches its maximum value (0.83) for a ΔH threshold of 1.0 km. The latter is associated to a POD score of 0.95 and to a FAR of 0.13. For the DOH 35-dBZ and 45-dBZ methods, CSI score maximizes for the same height difference threshold (1.0 km); a slight increase of FAR score for ΔH values > 1.5 km has been detected for both criteria.

As concerning the VLD method, the results obtained for the three VLD criteria tested in this study (VLDa, VLDb and VLDc) are presented in Fig. 5. The latter shows that the CSI score (0.80) found for VLDa is higher than those discovered for the other two criteria (0.74 for VLDb and 0.77 for VLDc). For VLDa criterion, the best CSI value corresponds to a threshold of 2.4 g m^{-3}, which correctly identifies all of the hail producing thunderstorms (POD = 1.0). However, the FAR score carried out for this criterion (0.20) is higher than that discovered for the DOH

Table 2
For every thunderstorm event belonging to the training dataset, the following information are displayed: date (yyyy/mm/dd), time (in UTC), distance from the radar site (R) of the on-ground observation, altitude of the highest echo detected by radar (H_{TOP}), freezing level (H_{T0}), maximum altitude of the 35-dBZ (H_{Z35}), 40-dBZ (H_{Z40}) and 45-dBZ (H_{Z45}) reflectivity cores and VLD values derived from VLDa, VLDb and VLDc products. The information not available are indicated as "n.a.". H_{TOP}, H_{Z35}, H_{Z40}, H_{Z45}, VLDa, VLDb and VLDc values have been computed within 15-km distance from the location where the on-ground observation of thunderstorm event has been reported. The dates in which hail precipitation has been observed hail events are marked by an asterisk.

Date	Time (UTC)	R (km)	H_{TOP} (km)	H_{T0} (km)	H_{Z35} (km)	H_{Z40} (km)	H_{Z45} (km)	VLDa ($g\,m^{-3}$)	VLDb ($g\,m^{-3}$)	VLDc ($g\,m^{-3}$)
2012/04/17*	07:45	7.5	4.2	2.0	3.2	3.1	3.0	4.0	4.6	5.0
2012/05/28*	09:30	26.2	7.5	2.7	4.8	4.0	3.3	3.2	3.7	3.8
2012/05/09*	19:35	15.8	5.6	3.6	3.8	3.5	3.7	6.4	7.3	8.4
2012/10/27	10:45	11.0	4.8	3.0	3.2	3.0	n.a.	1.9	2.2	1.9
2012/10/27	11:10	26.4	7.5	3.0	6.1	5.1	6.4	3.4	4.6	5.5
2012/10/27	14:35	48.1	11.4	3.0	5.9	5.5	4.9	2.5	3.0	2.7
2012/11/28*	20:55	6.5	4.0	2.4	3.2	3.1	n.a.	5.3	5.8	7.3
2012/11/29*	15:35	15.7	5.6	1.7	4.4	4.4	3.3	3.1	3.6	3.9
2012/11/30*	09:35	11.3	4.8	1.4	3.1	3.0	3.0	3.6	4.0	4.9
2012/12/04	12:10	20.3	6.4	1.7	3.3	2.4	2.3	1.7	3.2	3.7
2013/01/14*	06:15	26.2	7.5	1.5	3.8	3.0	2.9	3.8	7.4	12.3
2013/01/14*	12:55	6.5	4.0	1.5	3.3	3.0	2.8	3.8	4.3	4.8
2013/01/14*	13:55	20.3	6.4	1.5	4.2	3.9	3.0	2.6	3.0	3.2
2014/11/12	18:30	26.4	7.5	2.8	3.1	3.2	2.8	1.7	3.5	5.0
2014/11/15	23:05	11.0	4.8	3.2	4.0	3.7	4.2	2.2	2.6	2.4
2014/11/26	13:10	7.4	4.1	2.6	2.7	3.0	n.a.	2.0	2.0	1.8
2014/12/03	16:15	11.0	4.8	2.5	3.5	3.3	3.0	2.6	3.1	3.0
2014/12/05	10:55	32.4	8.6	2.2	3.5	3.0	3.0	3.4	4.0	3.8
2014/12/05	14:15	11.0	4.8	2.2	3.1	3.1	3.2	3.7	4.6	5.9
2014/12/16*	08:55	7.5	4.2	2.0	3.0	3.0	3.0	4.1	5.2	6.1
2014/12/16*	12:40	4.2	3.6	2.0	3.5	3.5	3.4	3.2	4.2	5.3
2015/01/18*	07:30	12.8	5.1	1.7	3.8	3.5	3.5	2.4	2.8	2.9
2015/02/03*	18:55	2.8	3.3	1.0	2.3	2.8	1.6	2.9	3.4	3.4
2015/02/15*	15:05	28.0	7.8	1.2	2.9	2.9	2.7	2.9	3.5	3.2
2015/03/27*	13:20	29.6	8.1	2.3	6.6	6.4	6.2	2.9	3.3	3.8
2015/06/07*	14:35	35.0	9.1	3.6	8.4	8.0	7.8	4.0	4.3	5.3
2015/06/07*	15:10	32.4	8.6	3.6	8.5	8.4	8.4	3.8	4.2	6.5
2015/06/08*	15:00	29.4	8.1	3.4	7.1	7.1	6.4	2.5	4.4	4.8
2015/06/09*	13:50	50.2	11.8	3.4	9.3	9.1	9.1	5.1	2.8	3.8
2015/06/09*	15:30	10.6	4.7	3.4	4.7	4.7	4.5	3.8	4.5	5.0
2015/06/10	14:25	53.9	12.4	3.5	6.2	5.0	4.6	1.2	1.3	1.6

40-dBZ algorithm. The VLD warning threshold for hail events established in this work differs in a significant way from those determined in the previous studies (e.g., Amburn and Wolf, 1997; Lahiff, 2005; Roeseler and Wood, 2001; Rose and Troutman, 1997). The latter, in fact, have revealed that the VLD threshold values, which correctly discriminate between hailfall and rain, range between 3.1 and 3.7 $g\,m^{-3}$. Therefore, the present work stresses the importance to perform a local study, in order to make an optimal and reliable use of VLD tool for hail detection purposes.

The CMB criterion has been implemented using the outcomes of DOH 40-dBZ and VLDa methods as predictor variables. As first step, we have computed the average vectors and the covariance matrices for the two different classes, *HE* and *NHE* (Table 4). Then, we have calculated the pooled covariance matrix, according to Eq. (4) and, finally, the coefficients of the linear model, $\beta_1 = 0.9514$ and $\beta_2 = 1.2595$. Therefore, for each thunderstorm event belonging to the training events, the LDA estimator Φ has been determined according to the following equation:

$$\Phi = 0.9514\,(\Delta H) + 1.2595\,(VLD) \quad (11)$$

The behaviour of the scoring parameters for different thresholds of Φ is presented in Fig. 6a. The best CSI value (0.86) has been observed for $\Phi = 5.2$. This threshold identifies the 95% of the hail producing thunderstorms (POD = 0.95) and is associated to a FAR score (0.09) lower than the one found for the canonical techniques.

The HFOD criterion has been developed using as input variables the outcomes of DOH 40-dBZ and VLDa techniques. In order to optimize the inference function, for every parameter involved in Eq. (9) a research interval has been defined (Table 5), according to the results achieved in the framework of statistical analysis. For every possible combination of the six parameters listed in Table 5, the inference function has been compared with the ground truth hail reports using the contingency table described in Section 3.5. More specifically, it has been assumed that a hail event is detected by the inference function, when $M(\Delta H, VLD)$ is above a certain threshold. The contingency table has been computed for several values of the inference function, ranging from 0.0 to 1.0. The best results in terms of CSI have been achieved when $M_{OPT}(\Delta H, VLD)$ from Eq. (9) has been calculated with the following parameters: $w_1 = 0.5$, $w_2 = 0.5$, $\Delta H_1 = 0.4$ km, $\Delta H_2 = 1.4$ km, $VLD_1 = 1.4\ g\,m^{-3}$ and $VLD_2 = 2.4\ g\,m^{-3}$. Using these values, the

Table 3
For the thunderstorm events belonging to the training data set, the median values of the freezing level (H_{T0}) and of the outcomes of DOH and VLD criteria tested in this study are presented. To emphasize the seasonal variability of thunderstorm features, the results obtained for warm season events (May to October) and for cold season events (November to April) are shown.

Events occurred in 2012–2015 period	H_{T0} (m)	H_{Z35}-H_{T0} (m)	H_{Z40}-H_{T0} (m)	H_{Z45}-H_{T0} (m)	VLDa ($g\,m^{-3}$)	VLDb ($g\,m^{-3}$)	VLDc ($g\,m^{-3}$)
Warm season events (May to October)	3400	2900	2100	1900	3.4	4.2	4.8
Cold season events (Nov. to April)	2000	1400	1300	1200	3.0	3.6	3.9

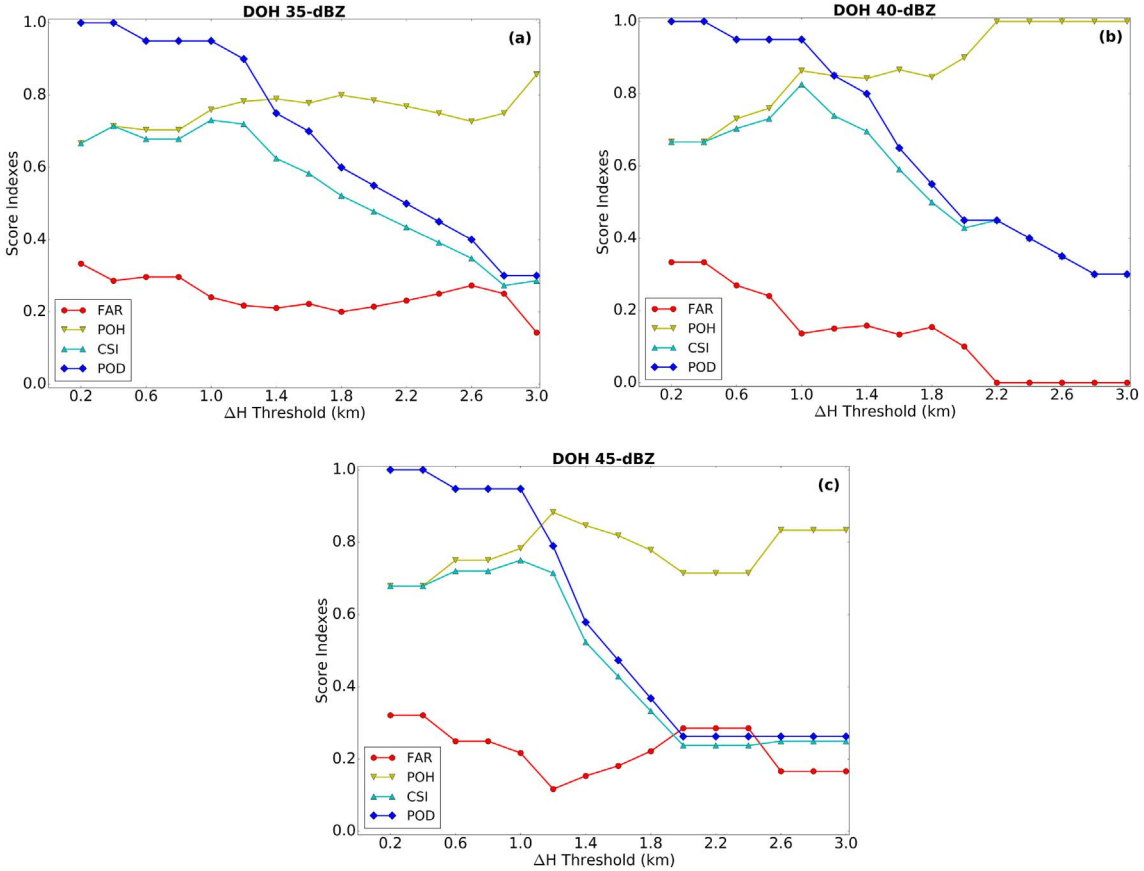

Fig. 4. The scoring parameters (FAR, POH, CSI and POD) for the DOH hail detection method as a function of the warning threshold. In (a), (b) and (c), the results obtained using the three reflectivity cores (35, 40 and 45 dBZ) tested in this study to compute ΔH are presented. The scoring parameters are deduced from the comparison of DOH method outcomes with ground-truth verification data.

maximum CSI (0.86) has been obtained for $M_{OPT} = 0.8$. This threshold is associated to a FAR of 0.09 and to a POD of 0.95, as shown in Fig. 6b.

4.2. Probability-of-hail indexes

In order to determine a POH index, that could be used into an operative framework, the relationship between POH score and the radar products ($\Delta H = H_{Z40} - H_{T0}$ for DOH 40-dBZ method and VLD for VLDa technique) has been modelled by using a third-order polynomial fit. The latter has been set up using POH score as dependent variable and the radar product (ΔH or VLD) as independent variable:

$$POH_{DOH\ 40-dBZ} = \sum_{i=1}^{4} g_i \Delta H^{i-1} \tag{12}$$

$$POH_{VLD_a} = \sum_{i=1}^{4} d_i VLD^{i-1} \tag{13}$$

For DOH 40-dBZ methodology, the best fit between ΔH thresholds and POH score has been obtained when $g_4 = 0.03595$, $g_3 = -0.164$, $g_2 = 0.3532$ and $g_1 = 0.5812$ (Fig. 7a). For VLDa method, the best fit has been achieved when $d_4 = 0.07278$, $d_3 = -0.5623$, $d_2 = 1.483$, $d_1 = -0.5395$ (Fig. 7b). Using the warning thresholds identified in the framework of statistical analysis (ΔH = 1.0 km and VLD = 2.4 g m^{-3}), the two optimal values for hail warning in Naples urban area have been determined, $POH_{DOH\ 40-dBZ} = 0.81$ and $POH_{VLDa} = 0.79$. Therefore, for DOH 40-dBZ method, when $POH_{DOH\ 40-dBZ}$ is equal or > 0.81 (81% in percentage), a hail event is detected. In the same manner, for VLDa method, when POH_{VLDa} is equal or > 0.79 (79% in percentage), hailfall is occurring.

The POH index for CMB criterion (POH_{CMB}) has been determined using the same heuristic approach. The best fit between POH score and Φ has been achieved through a two-order polynomial model (Fig. 7c):

$$POH_{CMB} = c_1\Phi^2 + c_2\Phi + c_3 \tag{14}$$

where the regression coefficients are $c_1 = -0.007117$, $c_2 = 0.1326$, $c_3 = 0.3977$. When POH_{CMB} is above 0.89 (89% in percentage), hail is assumed to occur. The hail-alert threshold just mentioned has been obtained evaluating the Eq. (14) for Φ = 5.2.

The combination of ΔH and VLD is also common to the fuzzy-logic POH index, hereafter, POH_{HFOD}, which can be simply obtained by:

$$POH_{HFOD} = M_{OPT}(\Delta H, VLD) = 0.5M_{\Delta H}(\Delta H, 0.4, 1.4) + 0.5M_{VLD}(VLD, 1.4, 2.4) \tag{15}$$

As discussed in Section 4.1, when POH_{HFOD} is larger than 0.8 (80% in percentage), a hail event is detected by the radar.

A summary of the four different methods to compute the POH is given in Table 6, together with the relative warning threshold T_{POH} (i.e. HAIL/No HAIL threshold). It is worth mentioning that all POH determined with the four methods are computed in each pixel (*i*, *j*) of the radar domain at each time step t_n.

The probability of hail (POH), using single-polarization X-band weather radar data, can be also used labelling each pixel (*i*, *j*) in the radar domain, at each the time step of the volume scan t_n, as follow:

$$L_{POH}(i,j,t_n) = \begin{cases} \text{"HAIL"} & \text{if } POH(i,j,t_n) \geq T_{POH} \\ \text{"NO HAIL"} & \text{if } 0 \leq POH(i,j,t_n) < T_{POH} \end{cases} \tag{16}$$

In Eq. (16), the term POH(*i*, *j*, t_n) represents the areal probability of hail detection applied to all pixels (*i*, *j*) within the radar coverage at each discrete time step of the volume scan t_n. Its value depends of the

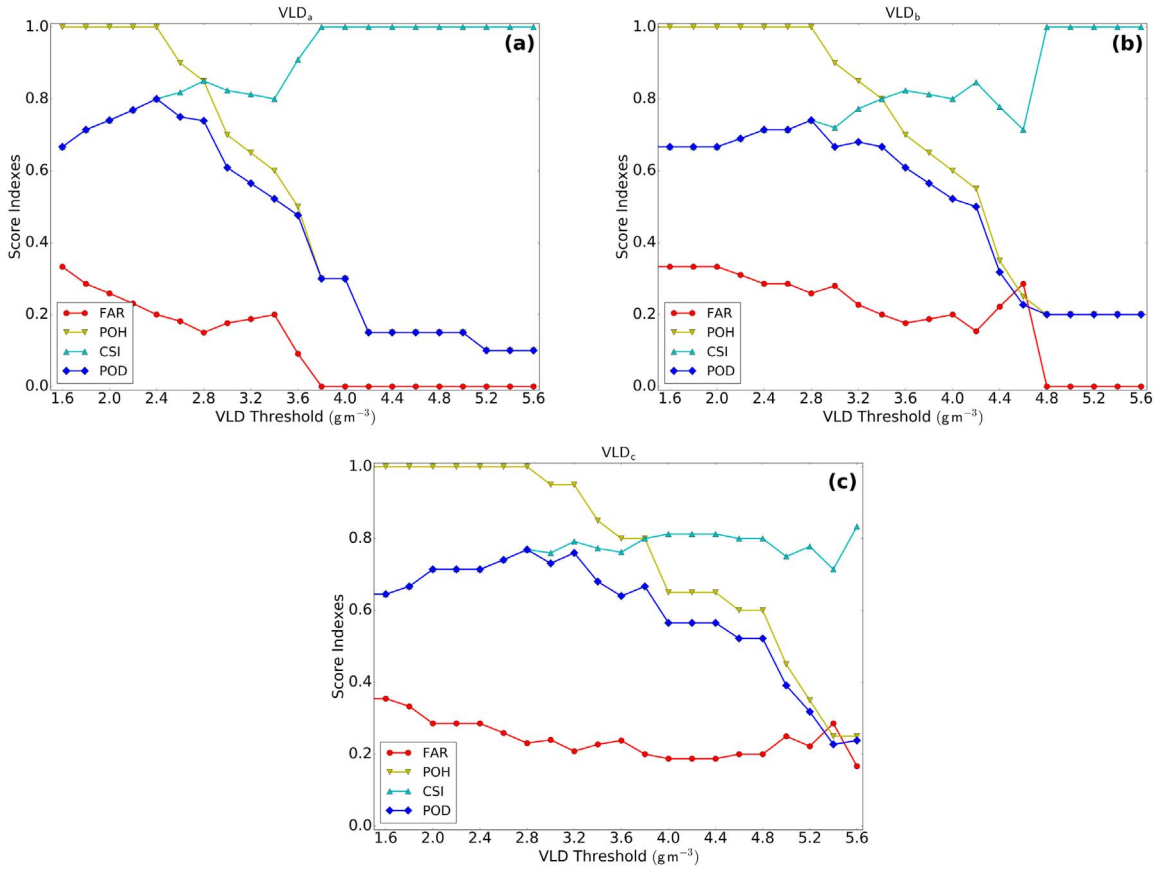

Fig. 5. The scoring parameters (FAR, POH, CSI and POD) for the VLD hail detection method as a function of the warning threshold. In (a), (b) and (c), the results obtained using the three different VLD products (VLDa, VLDb and VLDc) tested in this study are presented. The three VLD products differ for the set of coefficients (*a*, *b*) used in the conversion relationship between radar reflectivity measurements and liquid water content. The scoring parameters are deduced from the comparison of VLD technique output with ground-truth verification data.

Table 4
For each of the two event classes, hail (*HE*) and no-hail (*NHE*), involved in the application of CMB method, the values of the means vectors, μ_{HE} and μ_{NHE}, and of the two covariance matrices, C_{HE} and C_{NHE}, are presented. The statistics have been computed with respect to the training dataset, using ΔH ($= H_{Z40} - H_{T0}$) and VLDa as predictors.

Class	Count	Statistics	ΔH (km)	VLDa (g m^{-3})
HE	$n_1 = 20$	Means vector (μ_{HE})	2.49	3.72
		Covariance matrix (C_{HE})	$\begin{bmatrix} 2.25 & -0.03 \\ -0.03 & 1.23 \end{bmatrix}$	
NHE	$n_2 = 11$	Means vector (μ_{NHE})	0.92	2.39
		Covariance matrix (C_{NHE})	$\begin{bmatrix} 0.42 & 0.16 \\ 0.16 & 0.66 \end{bmatrix}$	

techniques used (i.e., DOH 40-dBZ, VLDa; CMB and HFOD), whose T_{POH} threshold values are reported in Table 6. It is worth mentioning that the results of the four L_{POH} products can be very useful to easily identify the areas where a "Hail Risk" is expected, whereas POH(i, j, t_n) can identify the areas where the probability of hail is high.

4.3. Statistical tests and application to a case study

The test dataset has been used to assess independently the performance obtained from the various techniques. The results, in terms of the statistical scores presented in Eq. (10), are highlighted in Table 7. The HFOD criterion performs better than other criteria methods in terms of both CSI and FAR, whereas the VLDa criterion exhibits the finest performance with respect to POD score.

The ROC curves obtained for the hail detection and probability products developed in this study are presented in Fig. 8. The results highlight that the combined criteria, HFOD and CMB, have the best predictive skills: they are characterized, in fact, by a ROC area value of 0.93 and 0.89, respectively (Table 7).

An example of application of the radar-based POH products developed in this study is presented for a severe hailstorm event, occurred on 21 July 2014.

4.3.1. Hail event occurred on 21 July 2014

On July 21, 2014 the coastal areas of the Campania region were affected by a strong convective activity. The 500-hPa geopotential height field (Fig. 9, left panel) reveals that the study area was located along the boundary of two different air masses. A through over the northern Italy, in fact, determined a cold air advection over the northern and central sectors of Italian peninsula and, at the same time, an advection of moist and warm air over southern Tyrrhenian sea. This thermal boundary was associated with some meteorological factors very favourable to the convection forcing in Mediterranean basins (Lebeaupin et al., 2006): a low-level wind convergence line, a jet-stream in the upper levels (Fig. 9, right panel) and a strong advection of moisture. Moreover, the convective activity was promoted by the high sea surface temperature (24 °C), which supplied moisture to the low-levels as well as increasing the convective instability. The isotherm of zero degree, according to the sounding data of Pratica di Mare collected at 12:00 UTC, was roughly 3500 m above the sea level.

In the afternoon hours, a strong hailstorm affected the Sorrentine Peninsula, a region that separates the Gulf of Naples to the north from the Gulf of Salerno to the south. The reflectivity volumes collected by WR-10X, presented in Fig. 10 in terms of Vertical Maximum Intensity (i.e. the highest reflectivity value on the vertical of every radar bin), allow tracking the displacement of the convective cell. The latter, after showing its first signature on WR-10X images at 14:35 UTC, moved

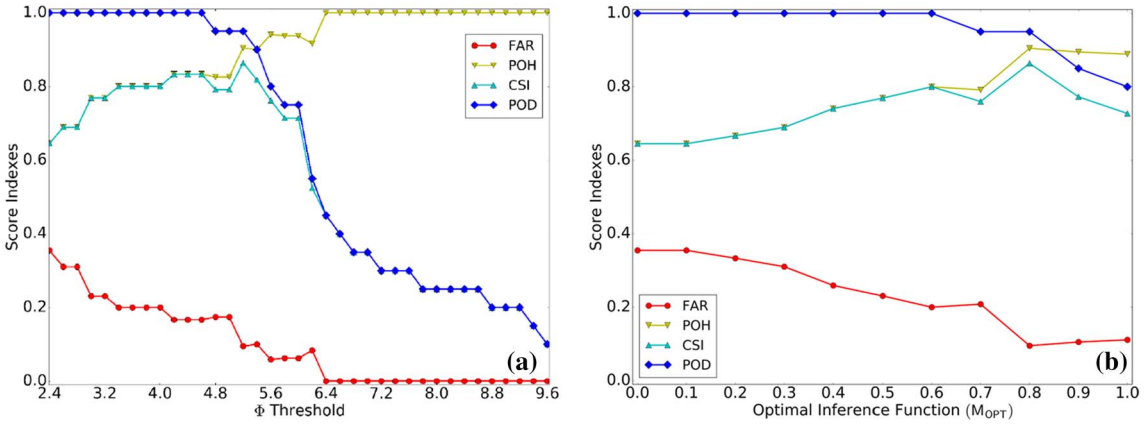

Fig. 6. Behaviour of the scoring parameters (FAR, POH, CSI and POD) for different thresholds of the two combined methods. In panel (a) the results obtained for CMB criterion are shown, whereas in panel (b) those achieved for the HFOD criterion are presented. The scoring parameters are deduced from the comparison of CMB and HFOD outcomes with ground-truth verification data.

Table 5
Research interval (minimum value, maximum value and step) of the six parameters (w_1, w_2, ΔH_1, ΔH_2, VLD_1 and VLD_2) involved in the computation of the inference function M (ΔH, VLD).

Parameter	Minimum value	Maximum value	Step
w_1	0.0	1.0	0.1
w_2	0.0	1.0	0.1
ΔH_1 (km)	0.2	0.9	0.1
ΔH_2 (km)	0.9	2.0	0.1
VLD_1 (g m^{-3})	1.4	2.3	0.1
VLD_2 (g m^{-3})	2.3	3.3	0.1

from southwest to northeast, affecting the Sorrentine Peninsula (whose position is marked by a black circle in Fig. 10a). The convective system approached the city of Sorrento at 15:25 UTC, exhibiting, according to the Meteosat Second Generation (MSG) infrared satellite image (Fig. 11, left panel), a V-shaped structure. The thunderstorm produced a strong hail precipitation, which lasted about 15 min. According to local newspapers (Il Mattino, July, 21, 2014; Positano News, 2014 July 21a), the hailstones had a relevant diameter (up to 3–4 cm, see Fig. 11, right panel) and caused serious damages to plants, crops and transport

Table 6
Summary of the four different methods to compute the POH together with the relative warning threshold (i.e. HAIL/No HAIL threshold).

Hail detection method	POH symbol	POH calculation	Threshold (T_{POH}) hail/no hail
DOH 40-dBZ	$POH_{DOH\ 40-dBZ}$	From Eq. (12)	0.81
VLDa	POH_{VLDa}	From Eq. (13)	0.79
CMB	POH_{CMB}	From Eq. (14)	0.89
HFOD	POH_{HFOD}	From Eq. (15)	0.80

activities.

Using Table 6, $POH_{DOH\ 40\text{-}dBZ}$, POH_{VLDa}, POH_{CMB} and POH_{HFOD} have been generated and shown in Fig. 12 as percentage. According to on-ground reports and observations, in the area of Sorrento a very high probability of hail has been detected above the alert thresholds. However, $POH_{DOH\ 40\text{-}dBZ}$ and POH_{VLDa} products have exhibited some difference in terms of extension of the hail-affected area. The POH_{VLDa}, in fact, has restricted the hail alert only to a part of the municipality of Sorrento and Massa Lubrense, whereas the $POH_{DOH\ 40\text{-}dBZ}$ index has detected a very high probability of hail (≅100%) also in the south-eastern sector of the Sorrentine Peninsula, at the boundary between the

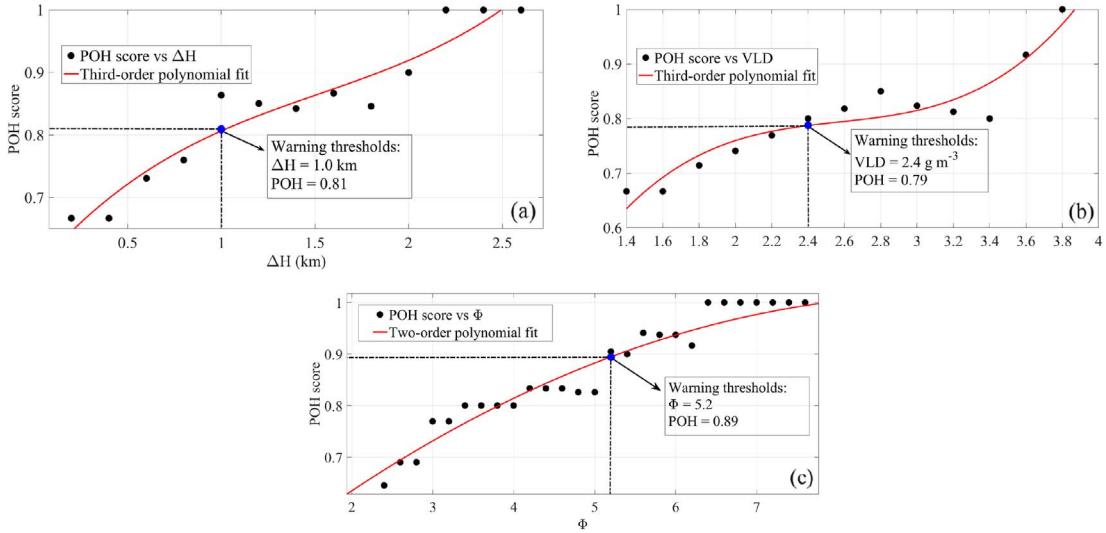

Fig. 7. The Probability of hail (POH) as a function of ΔH (a), which is the outcome of DOH 40-dBZ criterion, VLD (b), which is the output of VLDa method, and Φ (c), the outcome of CMB algorithm. The POH indexes, shown as red curves, have been obtained through an empirical approach, using polynomial regressions. The warning thresholds (i.e. the threshold above which hail is occurring) are indicated as blue filled circle over all three panels. (For interpretation of the references to color in this figure legend, the reader is referred to the web version of this article.)

Table 7
For each of the four radar-based hail detection methods (DOH 40-dBZ, VLDa, CMB and HFOD techniques) tested in this study, the statistical scores (CSI, FAR and POD) obtained for the warning threshold are presented. The HFOD criterion performs better in terms of CSI and FAR, whereas the VLDa technique exhibits the best performance for POD score. In the latter column, the area under ROC curve measured for the four different methodologies is also presented; an area of 1.0 represents a perfect test. The accuracy assessment of the hail detection algorithms developed in this study has been performed through an independent test dataset, which includes a sample of 22 thunderstorm events.

Hail detection method	Warning threshold	POD	FAR	CSI	Area under the ROC curve
DOH 40-dBZ	$\Delta H = 1.0$ km	0.86	0.07	0.80	0.83
VLDa	VLD = 2.4 g m^{-3}	1.00	0.30	0.70	0.82
CMB	$\Phi = 5.2$	0.93	0.21	0.74	0.89
HFOD	$M_{OPT} = 0.8$	0.86	0.00	0.86	0.93

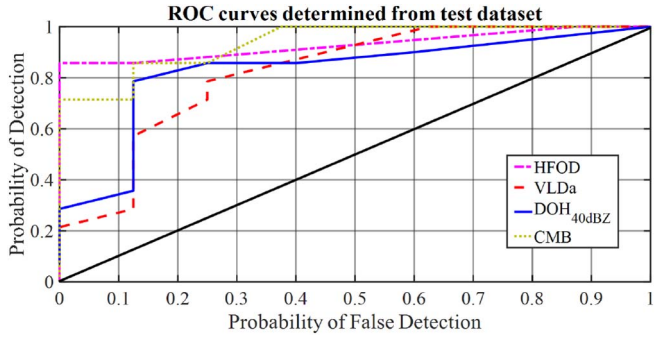

Fig. 8. Relative operating characteristic (ROC) curves for the four different hail detection and probability products developed in this works. The curves have been obtained plotting the Probability of False Detection (POFD) against the Probability of Detection (POD) score for different thresholds of the algorithms. The black diagonal line represents a completely uninformative test, corresponding to a ROC area of 0.5. The area under the curve can be considered a measure of how well a methodology is able to detect hail events. The four ROC curves have been obtained in the framework of the independent verification through the test dataset.

provinces of Naples and Salerno. However, none on-ground observation of hail has been reported in this area.

The POH_{HFOD} and POH_{CMB} index, besides to correctly identify the hail core in the city of Sorrento, help to better characterize the POH estimations where the POH_{VLDa} and the $POH_{DOH\ 40\text{-}dBZ}$ have given different results. Regarding the southeastern sector of Sorrentine Peninsula, in accordance with POH_{VLDa} product, the combined criteria have indicated a probability of hail below the warning threshold. At the same time, POH_{HFOD} and POH_{CMB}, in agreement with the $POH_{DOH\ 40\text{-}dBZ}$ index, have identified an area where hail is expected which includes not only the city of Sorrento, but also a portion of the western side of the Sorrentine Peninsula, which corresponds to the municipality of Massa Lubrense (whose location is highlighted by a black triangle in Fig. 12a). This result can be interpreted as a further evidence of POH_{HFOD} and POH_{CMB} indexes reliability. Although the ground truth reports provided by local newspaper (comprehensive of photographic and video material) have been all collected in Sorrento city, there is a reliable evidence that hail precipitation also affected the municipality of Massa Lubrense. As reported by local newspapers (Positano News, 2014 July 28b), in fact, this municipality has declared a state of natural disaster due to the huge damages and losses caused by hailfall on July 21, 2014.

5. Conclusions

This study has exploited the potentiality in hail detection and probability of a low-cost single-polarization X-band weather radar. The main novelties introduced by this work can be synthetized into the following two key-points: i) the advantages of the optimal combination of two radar-based hail detection techniques, based on different physical signatures, have been fully explored and synthetized within the powerful and flexible framework of fuzzy logic. ii) for the first time, a short-range single-polarization X-band has been used to generate an innovative experimental index of probability of hail (POH), tuned for an urban area; using this POH, the advantages of X-band systems, in terms of finer spatial-temporal resolution and affordable infrastructure, have been exploited.

The innovative method is based on an optimal combination, performed through the fuzzy-logic approach, of two well-known single-polarization radar-based hail detection techniques, the DOH algorithm and the VLD method. These two canonical methodologies have been adapted at the X-band and at the Naples' study area through a sensitivity analysis, which has involved a systematic comparison between their outcomes (ΔH, expressed in km, and VLD, expressed in g m^{-3}, respectively) and the on-ground observations of thunderstorm events. The training analysis has allowed determining, for both optimized DOH and VLD techniques, a warning threshold that discriminates between hail occurrence and no occurrence of hail, as well as a probability of hail (POH) index, that can be expressed as percentage, named respectively $POH_{DOH\ 40\text{-}dBZ}$ and POH_{VLDa}.

The two canonical hail detection products have been merged into

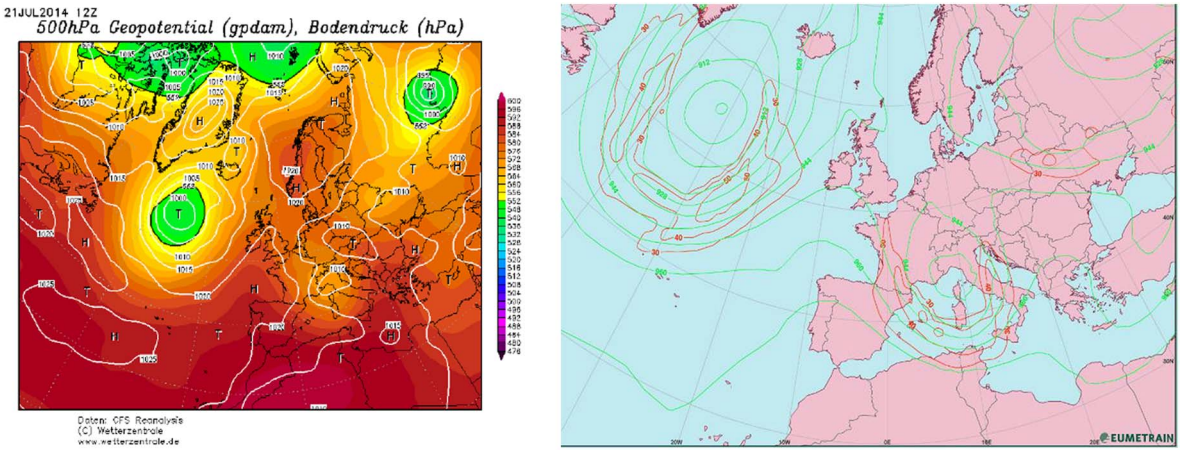

Fig. 9. In the left panel, the 500-hPa geopotential height (Z500) and sea-level pressure (SLP) analysis fields on 21 July 2014, 12:00 UTC are presented. In the right panel, for the same event, the 300-hPa geopotential height (Z300), shown as green isohypses and expressed in decametres (dam), and the 300-hPa wind speed (W300), shown as red isotaches and expressed in meters per second (m/s), are presented. The Z500 and SLP fields have been retrieved from Climate Forecast System (CFS) reanalysis archive (Saha et al., 2010) through the website http://www.wetterzentrale.de/de/reanalysis.php?map=1&model=cfsr&var=1, whereas the Z300 and W300 fields have been retrieved from EUMeTrain/ePort archive through the website http://eumetrain.org/eport.html. (For interpretation of the references to color in this figure legend, the reader is referred to the web version of this article.)

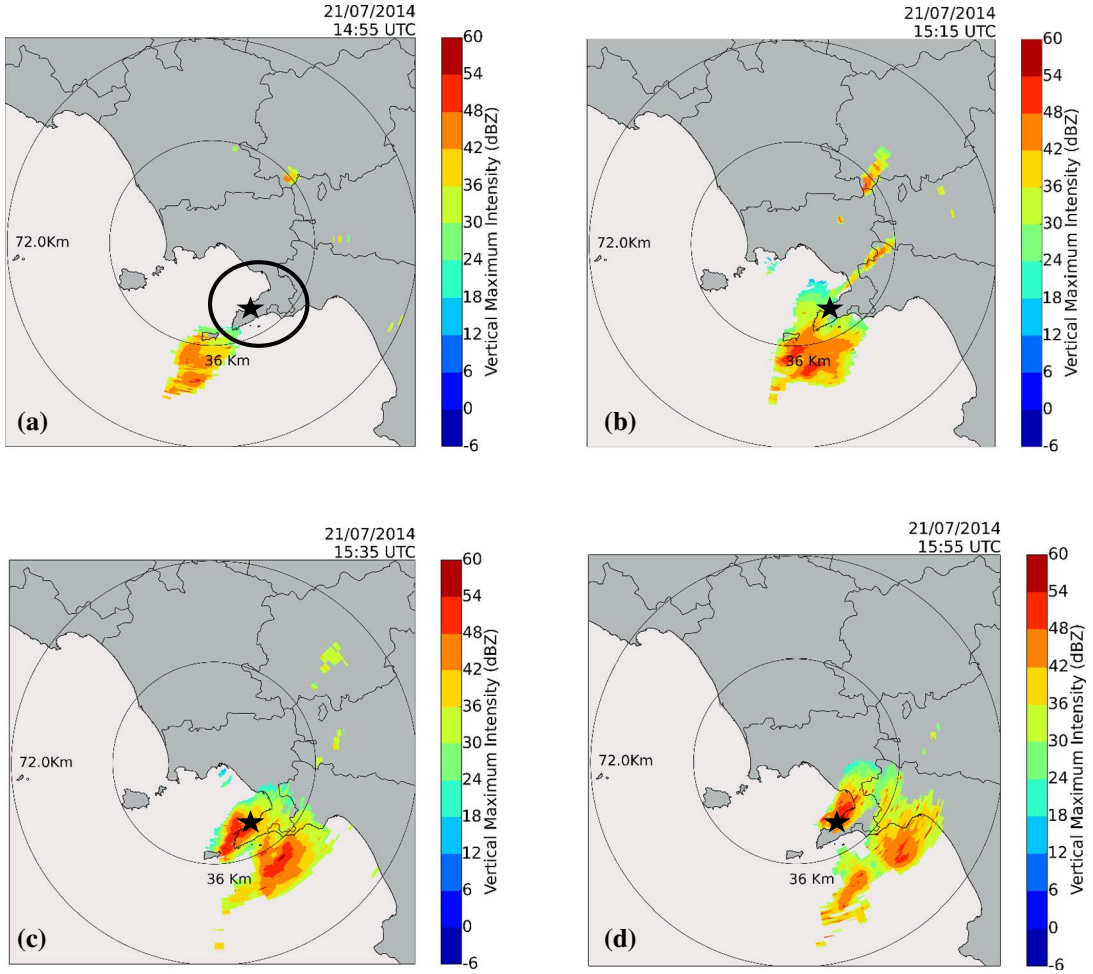

Fig. 10. WR-10X images showing the evolution of hailstorm that affected the city of Sorrento on 21 July 2014. Vertically Maximum Intensity (VMI) product obtained at 14:55 UTC (a), 15:15 UTC (b), 15:35 UTC (c) and 15:55 (d) is shown. The thunderstorm cell developed over Tyrrhenian Sea and then moved from south-western to north-eastern, affecting both the Gulf of Naples and the Gulf of Salerno. The Sorrentine Peninsula is highlighted by a black circle in panel (a). The black star marker indicates the location where hail precipitation on the ground has been observed.

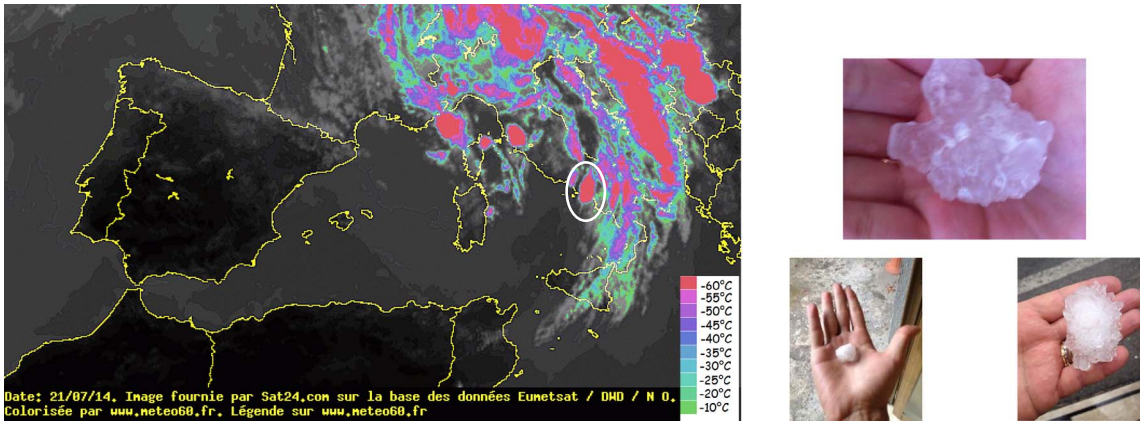

Fig. 11. In the left panel, a Meteosat Second Generation (MSG) infrared image showing cloud top temperature at 21 July 2014, 15:30 UTC is presented. The thunderstorm that caused hail precipitation in Sorrentine Peninsula is highlighted by a white circle. Satellite image courtesy of http://www.meteo60.fr/ and EUMETSAT. The cloud top temperature colorbar has been adapted from http://www.meteo60.fr/. The right panel shows three photographic evidences (retrieved from Positano News, 2014 July 21a) of the hailstones produced by convective cell that affected the city of Sorrento. (For interpretation of the references to color in this figure legend, the reader is referred to the web version of this article.)

two different combined POH indexes: the first one, named POH_{CMB}, is based on Linear Discriminant Analysis, whereas the second one, named POH_{HFOD}, has been designed through the fuzzy logic approach. Using the outcomes of the optimized DOH and VLD criteria as input variables of the fuzzy logic system, an inference function (M) has been determined means of a weighted linear combination of two ramp membership functions. In the framework of training verification analysis, the M function has been tested for several combinations of ΔH, VLD and weights values, in order to optimize its performance.

The skills of the four trained hail detection methods have been

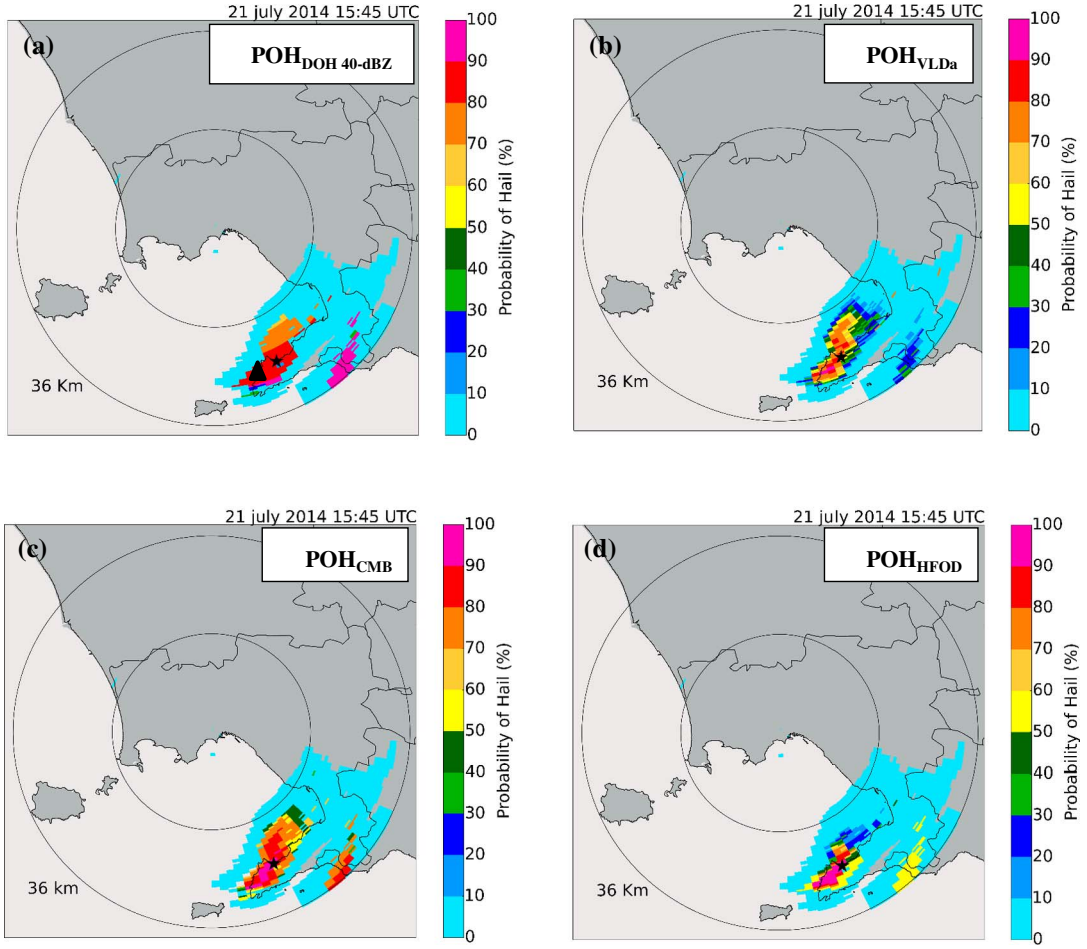

Fig. 12. Probability of hail indexes obtained by WR-10X for hailstorm occurred in the Sorrentine Peninsula on May 26, 2012 (15:45 UTC). In panels (a), (b), (c) and (d), $POH_{DOH\ 40\text{-}dBZ}$, POH_{VLDa}, POH_{CMB} and POH_{HFOD} maps are presented, respectively. To better display the thunderstorm core features in the area of interest, a zoom on the Gulf of Naples has been performed. The location of Sorrento city, where hailfall has been reported, is highlighted as black star, whereas the municipality of Massa Lubrense, where a state of natural disaster has been declared after the hail event, is indicated as black triangle in panel (a).

evaluated considering a separate test dataset, which includes 22 thunderstorm events. The introduction of the HFOD method determines an improvement of the statistical results with respect to the other methods evaluated in our study, in terms of FAR, CSI and ROC area. However, it should be pointed out that the results achieved in this study are not statistically significant at high confidence levels, due to the relatively small number of thunderstorm events considered. Therefore, future work shall be primarily devoted to enlarge the dataset used to train and test the proposed hail detection and probability criteria, in order to evaluate the possible benefits of the fuzzy-logic approach through a more robust statistical model.

An example of application of the radar-based hail detection products developed in this work has been shown for a relevant hailstorm, occurred on 21 July 2014. The analysed case, related to a strong hailfall observed in Sorrentine Peninsula, has clearly demonstrate the advantages introduced by the combined criteria, which have proved to be more reliable in identifying the area where severe hail damages have been reported.

The results achieved in this study are very promising and can bring benefits to the prevention of the hail-induced risks. However, during very strong convective conditions complete signal loss can occur, in which case correction with PIA iterative method is not possible at all and thus the developed hail algorithm cannot be applied in the whole radar selected domain (50 km of range). This is a limitation for its use in an operative framework and a real-time application is therefore excluded at the present time. On the other hand, the developed algorithms could be useful into operational context when the attenuation problem is solved or limited, like when utilizing a network of X-band radars and could be adapted to C and S band radars. In this respect, the detection of the signal extinction range, which is defined as the range where the backscatter signal is below the noise level due to severe rainfall attenuation, is another topic of interest. The signal extinction area can be identified in the radar map in order to mark the unknown areas where the method is not usable and may help to better assess the proposed technique (Maki et al., 2012). More PPI sweeps at higher elevation angles should be also included into the operational radar scanning strategy, in order to improve the hail detection products performance close to the radar site.

The quality of the on-ground observations used in this work is adversely affected by the inhomogeneity in spotters' spatial distribution. In order to improve the reliability of the proposed hail detection and probability products, the availability of other on-ground sources, such as the data provided by insurance companies and the lightning density, should be investigated. Future studies will be also focused on the development of two different HFOD criteria, one for warm season and the other one for cold season, in order to take into account the seasonal variability of the parameters involved in DOH method.

Acknowledgements

The authors are grateful to the “Soprintendenza Speciale per il Patrimonio Storico Artistico ed Etnoantropologico e per il Polo Museale

della città di Napoli" for hosting the weather radar at Castel Sant'Elmo. ELDES srl (Florence, Italy) personnel is acknowledged for the valuable technical support. The authors are also grateful to the administrator of the website http://www.meteo60.fr/ for having kindly grant the permission to reproduce a satellite image archived in the following section: http://archives.meteo60.fr/archives-sat.php#top. Moreover, the authors warmly thank the colleagues Dr. Saverio di Fabio (Centre of Excellence CETEMPS, University of l'Aquila) and Dr. Klaide De Sanctis (HIMET srl, l'Aquila, Italy) for having kindly provided the vertical temperature profiles predicted in the region of interest by the WRF model. The authors thank the two anonymous reviewers for their valuable comments and suggestions.

References

Alberoni, P.P., Andersson, T., Mezzasalma, P., Michelson, D.B., Nanni, S., 2001. Use of the vertical reflectivity profile for identification of anomalous propagation. Meteorol. Appl. 8 (3), 257–266.
Allen, J.T., Tippett, M.K., 2015. The characteristics of United States hail reports: 1955–2014. Electron. J. Severe Storms Meteorol. 10 (3), 1–31.
Amburn, S.A., Wolf, P.L., 1997. VIL density as a hail indicator. Weather Forecast. 12, 473–478.
Anagnostou, E.N., Anagnostou, M.N., Krajewski, W., Kruger, A., Miriovsky, B., 2004. High-resolution rainfall estimation from X-band polarimetric radar measurements. J. Hydrometeorol. 5, 110–128.
Auer, A.H., 1994. Hail recognition through the combined use of radar reflectivity and cloud-top temperatures. Mon. Weather Rev. 122, 2218–2221.
Aydin, K., Seliga, T.A., Balaji, V., 1986. Remote sensing of hail with a dual linear polarization radar. J. Appl. Meteorol. 25, 1475–1484.
Azorin-Molina, C., Connell, B.H., Baena-Calatrava, R., 2009. Sea-breeze convergence zones from AVHRR over the Iberian Mediterranean area and the Isle of Mallorca, Spain. J. Appl. Meteorol. Climatol. 48, 2069–2085.
Baumgart, L., Bass, E., Philips, B., Kloesel, K., 2008. Emergency management decision making during severe weather. Weather Forecast. 23, 1268–1279.
Bechini, R., Chandrasekar, V., 2015. A Semisupervised robust hydrometeor classification method for dual-polarization radar applications. J. Atmos. Ocean. Technol. 32, 22–47.
Bechini, R., Baldini, L., Chandrasekar, V., 2013. Polarimetric radar observations in the ice region of precipitating clouds at C-band and X-band radar frequencies. J. Appl. Meteorol. Climatol. 52 (5), 1147–1169.
Berenguer, M., Sempere Torres, D., 2012. Adding Value to the Measurements of an X − band Radar on Catalonian Coast. Meteorological Technology International, pp. 85–88 (August).
Bradley, A.P., 1997. The use of the area under the ROC curve in the evaluation of machine learning algorithms. Pattern Recogn. 30 (7), 1145–1159.
Brimelow, J.C., Reuter, G.W., Bellon, A., Hudak, D., 2004. A radar-based methodology for preparing a severe thunderstorm climatology in central Alberta. Atmosphere-Ocean 42 (1), 13–22.
Burgess, D.W., Lemon, L.R., 1990. Severe thunderstorm detection by radar. In: Radar in Meteorology. American Meteorological Society, pp. 619–647.
Capozzi, V., Picciotti, E., Budillon, G., Marzano, F.S., 2014. X-band weather radar monitoring of precipitation fields in Naples urban areas: data quality, comparison and analysis. In: The Eighth European Conference on Radar in Meteorology and Hydrology.
Capozzi, V., Mazzarella, V., Moccia, M., Picciotti, E., Budillon, G., Marzano, F.S., 2015. Hail detection in Naples urban area using single-polarization X-band weather radar: preliminary results. In: Metrology for Aerospace (MetroAeroSpace), 2015 IEEE Xplore Digital Library, pp. 289–294.
Capozzi, V., Picciotti, E., Mazzarella, V., Budillon, G., Marzano, F.S., 2016. Hail storm hazard in urban areas: identification and probability of occurrence by using a single-polarization X-band weather radar. Hydrol. Earth Syst. Sci. Discuss. http://dx.doi.org/10.5194/hess-2016-177.
Ceperuelo, M., Ribas, T.R., LlsatBotuja, M.C., Sanchez, J.L., 2009. Improving hail identification in the Ebro Valley region using radar observations: probability equations and warning thresholds. Atmos. Res. 93, 474–482.
Chandrasekar, V., Keränen, R., Lim, S., Moisseev, D., 2013. Recent advances in classification of observations from dual polarization weather radars. Atmos. Res. 119, 97–111.
Changnon, S.A., 2001. Damaging thunderstorm activity in the United States. Bull. Am. Meteorol. Soc. 82, 597–608.
Delobbe, L., Holleman, L., 2006. Uncertainties in radar echo top heights used for hail detection. Meteorol. Appl. 13, 361–374.
Delobbe, L., Dehenauw, D., Hamid, K., Heméghaire, G., 2003. Hail Detection Using Radar Observations: Case Studies in the Summer 2002. Royal Meteorological Institute of Belgium.
Delrieu, G., Hucke, L., Creutin, J.D., 1999a. Attenuation in rain for X- and C-band weather radar systems: sensitivity with respect to the drop size distribution. J. Appl. Meteorol. 38, 57–68.
Delrieu, G., Serrar, S., Guardo, E., Creutin, J.D., 1999b. Rain measurement in hilly terrain with X-band weather radar systems: accuracy of path-integrated attenuation estimates derived from mountain returns. J. Atmos. Ocean. Technol. 16, 405–416.
Donavon, R.A., Jungbluth, K.A., 2007. Evaluation of a technique for radar identification of large hail across the Upper Midwest and Central Plains of the United States. Weather Forecast. 22, 244–254.
Doswell III, C.A., Edwards, R., Thompson, R.L., Hart, J.A., Crosbie, K.C., 2006. A simple and flexible method for ranking severe weather events. Weather Forecast. 21 (6), 939–951.
Dotzek, N., Groenemeijer, P., Feuerstein, B., Holzer, A.M., 2009. Overview of ESSL's severe convective storms research using the European Severe Weather Database ESWD. Atmos. Res. 93 (1), 575–586.
Erdin, R., Frei, C., Künsch, H.R., 2012. Data transformation and uncertainty in geostatistical combination of radar and rain gauges. J. Hydrometeorol. 13 (4), 1332–1346.
Farnell, C., Rigo, T., Martin-Vide, J., 2016. Application of cokriging techniques for the estimation of hail size. Theor. Appl. Climatol. 1–19.
Farnell, C., Rigo, T., Pineda, N., 2017. Lightning jump as a nowcast predictor: application to severe weather events in Catalonia. Atmos. Res. 183, 130–141.
Fawcett, T., 2006. An introduction to ROC analysis. Pattern Recogn. Lett. 27, 861–874.
Figueras i Ventura, J., Honoré, F., Tabary, P., 2013. X-band polarimetric weather radar observations of a hailstorm. J. Atmos. Ocean. Technol. 30, 2143–2151.
Fisher, R.A., 1936. The use of multiple measurements in taxonomic problems. Ann. Eugenics 7 (2), 179–188.
Fulton, R.A., Breidenbach, J.P., Seo, D., Miller, D., O'Bannon, T., 1998. The WSR-88D rainfall algorithm. Weather Forecast. 13, 377–395.
Gatlin, P., Goodman, S., 2010. A Total lightning trending algorithm to identify severe thunderstorms. J. Atmos. Ocean. Technol. 27, 3–22.
Geotis, S.G., 1963. Some radar measurements of hailstorms. J. Appl. Meteorol. 2, 270–275.
Greene, D.R., Clark, R.A., 1972. Vertically integrated liquid water – a new analysis tool. Mon. Weather Rev. 100, 548–552.
Han, L., Fu, S., Zhao, L., Zheng, Y., Wang, H., Lin, Y., 2009. 3D convectivestorm identification, tracking, and forecasting: an enhanced-TITANalgorithm. J. Atmos. Ocean. Technol. 26, 719–732.
Handwerker, J., 2002. Cell tracking with TRACE3D—a new algorithm. Atmos. Res. 61, 15–34.
Heinselman, P.L., Ryzhkov, A.V., 2006. Validation of polarimetric hail detection. Weather Forecast. 21, 839–850.
Hohl, R., Schiesser, H.H., Knepper, I., 2002. The use of weather radars to estimate hail damage to automobiles: an exploratory study in Switzerland. Atmos. Res. 61, 215–238.
Holleman, I., 2001. Hail detection using single-polaritazion radar. Sci. Report (KNMI WR-2001-01).
Il Mattino newspaper, 2014 July 21. Grandinata Record a Sorrento, i chicchi enormi danneggiano i campi. from. http://www.ilmattino.it/napoli/cronaca/grandinata_sorrento_foto_video-508584.html.
Kahraman, A., Tilev-Tanriover, S., Kadioglu, M., Schultz, D.M., Markowski, P.M., 2016. Severe hail climatology of Turkey. Mon. Weather Rev. 144, 337–346.
Kessinger, C.J., Brandes, E.A., Smith, J.W., 1995. A comparison of the NEXRAD and NSSL hail detection algorithms. In: 27th Conference on Radar Meteorology. AMS, pp. 603–605.
Komendantova, N., Mrzyglocki, R., Mignan, A., Khazai, B., Wenzel, F., Patt, A., Fleming, K., 2014. Multi-hazard and multi-risk decision-support tools as a part of participatory risk governance: feedback from civil protection stakeholders. Int. J. Disaster Risk Reduct. 8, 50–67.
Koussis, A.D., Lagouvardos, K., Mazi, K., Kotroni, V., Sitzmann, D., Lang, J., Zaiss, H., Buzzi, A., Malguzzi, P., 2003. Flood forecasts for urban basin with integrated hydro-meteorological model. J. Hydrol. Eng. 8 (1), 1–11.
Kunkel, K.E., Karl, T.R., Brooks, H., Kossin, J., Lawrimore, J.H., Arndt, H., Bosart, L., Changnon, D., Cutter, S.L., Doesken, N., Emanuel, K., Groisman, P.Y., Katz, R.W., Knutson, T., O'Brien, J., Paciorek, C.J., Peterson, T.C., Redmond, K., Robinson, D., Trapp, J., Vose, R., Weaver, S., Wehner, M., Wolter, K., Wuebbles, D., 2013. Monitoring and understanding trends in extreme storms: state of knowledge. Bull. Am. Meteorol. Soc. 94, 499–514.
Kunz, M., Kugel, P.I.S., 2015. Detection of hail signatures from single-polarization C-band radar reflectivity. Atmos. Res. 2015 (153), 565–577.
Lahiff, C.N., 2005. Vertically Integrated Liquid Density and its associated hail size range across the Burlington, Vermont County warning area. In: Eastern Region Technical Attachment, No. 05-01.
Lai, E.S.T., 1999. TREC application in tropical cyclone observation. In: Proc. ESCAP/WMO Typhoon Committee Annual Review. The Typhoon Committee, Seoul, South Korea, pp. 135–139.
Lakshmanan, V., Hondl, K., Potvin, C., Preignitz, D., 2013. An improved method for estimating radar echo-top height. Weather Forecast. 28, 481–488.
Lebeaupin, C., Ducrocq, V., Giordani, H., 2006. Sensitivity of torrential rain events to the sea surface temperature based on high-resolution numerical forecasts. J. Geophys. Res. 111 (D12), 1211.
Lemon, L.R., 1998. The radar "three-body scatter spike": an operational large-hail signature. Weather Forecast. 13, 327–340.
Li, L., Schmid, W., Joss, J., 1995. Nowcasting of motion and growth of precipitation with radar over a complex orography. J. Appl. Meteorol. 34, 1286–1300.
Liu, H., Chandrasekar, V., 2000. Classification of hydrometeors based on polarimetric radar measurements: development of fuzzy logic and neuro-fuzzy systems, and in situ verification. J. Atmos. Ocean. Technol. 17, 140–164.
Llasat, M.C., López, L., Barnolas, M., Llasat-Botija, M., 2008. Flash-floods in Catalonia: the social perception in a context of changing vulnerability. Adv. Geosci. 17, 63–70.
Llasat, M.C., Llasat-Botija, M., Barnolas, M., López, L., Altava-Ortiz, V., 2009. An analysis of the evolution of hydrometeorological extremes in newspapers: the case of Catalonia, 1982–2006. Nat. Hazards Earth Syst. Sci. 9 (4), 1201.

Löffler-Mang, M., Schön, D., Landry, M., 2010. Characteristics of a new automatic hail recorder. Atmos. Res. 100, 439–446.
Mahele, V.N., Zhang, G., Xue, M., 2014. Fuzzy logic classification of S-band polarimetric radar echoes to identify three-body scattering and improve data quality. J. Appl. Meteorol. Climatol. 53, 2017–2033.
Maki, M., Park, S.-G., Bringi, V.N., 2005. Effect of natural variations in rain drop size distributions on rain rate estimators of 3 cm wavelength polarimetric radar. J. Meteorol. Soc. Jpn. 83, 871–893.
Maki, M., Maesaka, T., Kato, A., Shimizu, S., Iwanami, K., 2012. Developing a composite rainfall map based on observations of an X-band polarimetric radar network and conventional C-band radar. Indian J. Radio Space Phys. 41, 461–470.
Marzano, F.S., Roberti, L., Di Michele, S., Tassa, A., Mugnai, A., 2003. Modeling of apparent radar reflectivity due to convective clouds at attenuating wavelengths. Radio Sci. 38, 1002.
Marzano, F.S., Scaranari, D., Vulpiani, G., 2007. Supervised fuzzy-logic classification of hydrometeors using C-band dual-polarized radars. IEEE Trans. Geosci. Remote Sens. 45, 3784–3799 (ISSN: 0196-2892).
Marzano, F.S., Botta, G., Montopoli, M., 2010. Iterative Bayesian retrieval of hydrometeor content from X-band polarimetric weather radar. IEEE Trans. Geosci. Remote Sens. 48, 3059–3074.
Marzano, F.S., Budillon, G., Picciotti, E., Montopoli, M., Zinzi, A., Buonocore, B., 2012. X-band weather radar monitoring real-time products in Rome and Naples urban areas. In: Proc. Of Tyrrhenian Workshop 2012 on Advances in Radar and Remote Sensing, Naples (Italy).
Mason, B.J., 1971. The Physics of Clouds. Clarendon Press, Oxford, UK.
Matrosov, S.Y., Kingsmill, D.E., Martner, B.E., Ralph, F.M., 2005. The utility of X-band polarimetric radar for quantitative estimates of rainfall parameters. J. Hydrometeorol. 6, 248–262.
Matrosov, S., Cifelli, R., Gochis, D., 2013. Measurements of heavy convective rainfall in the presence of hail in flood-prone areas using an X-band polarimetric radar. J. Appl. Meteorol. Climatol. 52, 395–407.
Mecikalski, J.R., Bedka, K.M., 2006. Forecasting convective initiation by monitoring the evolution of moving cumulus in daytime GOES imagery. Mon. Weather Rev. 134, 49–78.
Montopoli, M., Picciotti, E., Telleschi, A., Marzano, F.S., 2010. X-band weather radar monitoring of precipitation fields at urban scale: spatial calibration and accuracy evaluation. In: Proc. of the 6th European Conference on Radar in Meteorology and Hydrology (ERAD), Sibiu (Romania).
Morgan, G.M.J., Towery, N.G., 1975. Small-scale variability of hail and its significance for hail prevention experiments. J. Appl. Meteorol. 14, 763–770.
Nisi, L., Martius, O., Hering, A., Kunz, M., Germann, U., 2016. Spatial and temporal distribution of hailstorms in the Alpine region: a long-term, high resolution, radar-based analysis. Q. J. R. Meteorol. Soc. 142, 1590–1604. http://dx.doi.org/10.1002/qj.2771.
Park, H.S., Ryzhkov, A.V., Zrnic, D.S., Kim, K.-E., 2009. The hydrometeor classification algorithm for the polarimetric WSR-88D: description and application to an MCS. Weather Forecast. 24, 730–748.
Picciotti, E., Marzano, F.S., Anagnostou, E.N., Kalogiros, J., Fessas, Y., Volpi, A., Cazac, V., Pace, R., Cinque, G., Bernardini, L., De Sanctis, K., Montopoli, M., Anagnostou, M.N., Telleschi, A., 2013. Coupling X-band dual-polarized mini-radars and hydrometeorological forecast models: the HYDRORAD project. Nat. Hazards Earth Syst. Sci. 13 (5), 1229–1241.
Positano News, 2014 July 21a. Tempesta di grandine a Sorrento chicchi come noci Seiano allagata motorini trascinati a mare. Retrieved from. http://www.positanonews.it/articolo/140873/tempesta-di-grandine-a-sorrento-chicchi-come-noci-seiano-allagata-motorini-trascinati-a-mare-foto-video.
Positano News, 2014 July 28b. Sorrento grandinata del 21 luglio i comuni chiedono lo stato di calamità. Retrieved from. http://www.positanonews.it/articolo/141289/sorrento-grandinata-del-21-luglio-i-comuni-chiedono-lo-stato-di-calamita.
Price, C., Federmesser, B., 2006. Lightning-rainfall relationships in Mediterranean winter thunderstorms. Geophys. Res. Lett. 33, L07813. http://dx.doi.org/10.1029/2005GL024794.
Puskeiler, M., Kunz, M., Schmidberger, M., 2016. Hail statistics for Germany derived from single-polarization radar data. Atmos. Res. 178–179, 459–470.
Rigo, T., Pineda, N., 2016. Inferring the severity of a multicell thunderstorm evolving to supercell, by means of radar and total lightning. Electron. J. Severe Storms Meteorol. 11, 2.
Roberts, R., Burgess, D., Meister, M., 2006. Developing tools for nowcasting storm severity. Weather Forecast. 21, 540–558.
Roeseler, C.A., Wood, L., 2001. VLD Density and Associated Hail Size along the Northwest Gulf Coast. NWS Southern Region Local Research Project: Houston, TX and Lake Charles, LA.
Rose, M.A., Troutman, T.W., 1997. An Examination of VLD and Echo Top Associated With Large Hail in Middle Tennessee. NWS Southern Region Technical Attachment No. - 12 - 97-15. Nashville, TN.
Saha, S., et al., 2010. The NCEP climate forecast system reanalysis. Bull. Am. Meteorol. Soc. 91, 1015–1057.
Sánchez, J.L., Fraile, R., De La Madrid, J.L., De La Fuente, M.T., Rodriguez, P., Castro, A., 1996. Crop damage: the hail size factor. J. Appl. Meteorol. 35 (9), 1535–1541.
Schultz, C., Petersen, W., Carey, L., 2009. Preliminary development and evaluation of lightning jump algorithms for the real-time detection of severe weather. J. Appl. Meteorol. Climatol. 48, 2543–2563.
Schuster, S.S., Blong, R.J., Speer, M.S., 2005. A hail climatology of the greater Sydney area and New South Wales, Australia. Int. J. Climatol. 25 (12), 1633–1650.
Schuster, S.S., Blong, R.J., McAneney, K.J., 2006. Relationship between radar-derived hail kinetic energy and damage to insured buildings for severe hailstorms in Eastern Australia. Atmos. Res. 81 (3), 215–235.
Sieglaff, J.M., Hartung, D.C., Feltz, W.F., Cronce, L.M., Lakshmanan, V., 2013. A satellite-based convective cloud object tracking and multipurpose data fusion tool with application to developing convection. J. Atmos. Ocean. Technol. 30, 510–525.
Sioutas, M., Meaden, T., Webb, J.D., 2009. Hail frequency, distribution and intensity in Northern Greece. Atmos. Res. 93 (1), 526–533.
Skripniková, K., Řezáčová, K., 2014. Radar-based hail detection. Atmos. Res. 144, 175–185.
Straka, J.M., Zrnic, D.S., Ryzhkov, A.V., 2000. Bulk hydrometeor classification and quantification using polarimetric radar data. Synthesis of relations. J. Appl. Meteorol. 39 (8), 1341–1372.
Sun, J., Xue, M., Wilson, J.M., Zawadzki, I., Ballard, S.P., Onvlee-Hooimeyer, J., Joe, P., Barker, D.M., Li, P.W., Golding, B., Xu, M., Pinto, J., 2014. Use of NWP for nowcasting convective precipitation: recent progress and challenges. Bull. Am. Meteorol. Soc. 95, 409–426.
Tilford, K.A., Fox, N.I., Collier, C.G., 2002. Application of weather radar data for urban hydrology. Meteorol. Appl. 9 (Issue 1), 95–104.
Tuovinen, J.P., Punkka, A.J., Rauhala, J., Hohti, H., Schultz, D.M., 2009. Climatology of severe hail in Finland: 1930–2006. Mon. Weather Rev. 137 (7), 2238–2249.
Van de Beek, C.Z., Leijnse, H., Stricker, J.N.M., Uijlenhoet, R., Russchenberg, H.W.J., 2010. Performance of high-resolution X-band radar for rainfall measurement in The Netherlands. Hydrol. Earth Syst. Sci. 14, 205–221.
Villarini, G., Smith, J.A., Baeck, M.L., Sturdevant-Rees, P., Krajewski, W.F., 2010. Radar analyses of extreme rainfall and flooding in urban drainage basins. J. Hydrol. 381 (3), 266–286.
Vulpiani, G., Baldini, L., Roberto, N., 2015. Characterization of Mediterranean hail-bearing storms using an operational polarimetric X-band radar. Atmos. Meas. Tech. 8, 4681–4698.
Waldvogel, A., Federer, B., Grimm, P., 1979. Criteria for the detection of hail cells. J. Appl. Meteorol. 18, 1521–1525.
Weisman, M.L., Davis, C., Wang, W., Manning, K.W., Klemp, J.B., 2008. Experiences with 0–36-h explicit convective forecasts with the WRF-ARW model. Weather Forecast. 23, 407–437.
Witt, A., Eilts, M.D., Stumpf, G.J., Johnson, J.T., Mitchell, E.D., Thomas, K.W., 1998. An enhanced hail detection algorithm for the WSR-88D. Weather Forecast. 13, 286–303.
Wyatt, A., Witt, A., 1997. The effect of population density on ground-truth verification of reports used to score a hail detection algorithm. In: Preprints, 28th Conf. on Radar Meteorology, Austin, TX. Amer. Meteor. Soc.pp. 368–369.
Zrnić, D.S., 1987. Three-body scattering produces precipitation signature of special diagnostic value. Radio Sci. 22, 76–86.
Zrnić, D.S., Straka, J., Liu, Y., Vivekanandan, J., 2001. Testing a procedure for the automatic classification of hydrometeor types. J. Atmos. Ocean. Technol. 18, 892–913.

Web references

Archive of Meteosat Second Generation (MSG) Infrared Images. http://archives.meteo60.fr/archives-sat.php#top, Accessed date: 2 February 2017.
EUMeTrain/ePort Archive. http://eumetrain.org/eport.html, Accessed date: 2 March 2017.
Archive of Climate Forecast System (CFS) Reanalysis. www.wetterzentrale.de/de/reanalysis.php?map=1&model=cfsr&var=1, Accessed date: 2 February 2017.
Archive of spotters observations. www.campanialive.it, Accessed date: 1 February 2017.